Effect of biofouling roughness on the full-scale powering performance of a submarine

Dogancan Uzun*, Savas Sezen, Mehmet Atlar, Osman Turan

Department of Naval Architecture, Ocean and Marine Engineering, University of Strathclyde,100 Montrose Street, Glasgow, G4 0LZ, UK

*corresponding author; e-mail: dogancan.uzun@strath.ac.uk,

ABSTRACT

The aim of this study is to investigate the impact of barnacle type biofouling roughness on the full-scale powering performance of a submarine in calm seas. The importance of the diversified biofouling accumulations in terms of hull location is also examined over the submarine hull by implementing homogeneous and heterogenous roughness distribution. In this study, a Reynolds Averaged Navier Stokes (RANS) based CFD model was used for predicting the effects of biofouling roughness on the self-propulsion characteristics for the full-scale submarine form. The powering performance analyses are performed with discretised propeller geometry, and the Moving Reference Frame approach is used to model the rotational motion of the propeller. A proportional-integral (PI) approach is adopted to obtain the self-propulsion point efficiently by modifying the propeller's rotational speed. First, the resistance and the self-propulsion characteristics of the model scale submarine are validated with the experimental and other numerical studies in the literature. Following this validation task, a roughness function model is employed within a CFD software's wall function to represent the rough surfaces over the submarine hull. The results showed that although roughness has a varying effect on the submarine's self-propulsion characteristics depending on the roughness distribution, it increases the hull resistance and, hence, the delivered power overall. Roughness on the forward section of the hull has a more pronounced effect on the resistance and delivered power. The study demonstrated that the presence of partial hull fouling should not be ignored, and required precautions should be taken to prevent losses in submarine performance, especially for the fouling at the forward section of the submarine.

This is a peer-reviewed, accepted author manuscript of the following article: Uzun, D., Sezen, S., Atlar, M., & Turan, O. (2021). Effect of biofouling roughness on the full-scale powering performance of a submarine. Ocean Engineering, 238, [109773]. https://doi.org/10.1016/j.oceaneng.2021.109773

1 INTRODUCTION

Biofouling accumulation on ships causes deterioration in the hull's surface smoothness, which, in turn, results in increased frictional resistance. Therefore, surface roughness results in either increased power to maintain a service speed or a reduced speed at provided power, leading to economic and environmental penalties (Denny, 1951; Kempf, 1936; Schultz, 2007; Townsin, 2003). Biofouling growth rate and species in the fouling fauna depends on many factors, including idle time-frequencies, ship operational profile, ship speed, the efficiency of the fouling control coating and environmental factors (e.g. sea surface temperature, salinity, nutrients abundance and light) (Uzun et al., 2019). Davidson et al., (2009) stated that fouling accumulation on containerships might be limited and likely be fouled with only biofilm and algae since containerships have comparatively high speeds and short idle periods. On the other hand, slow speed ships with long port durations or naval vessels and submarines in a static state for long periods may show a wide variety of fouling fauna, including micro and macro fouling together.

The effect of surface roughness, whether due to coating, biofouling or mechanical roughness such as welding seams, on ship performance has received much attention so far in the literature (Andersson et al., 2020; Farkas et al., 2021; García et al., 2020; Murphy et al., 2018; Schultz et al., 2011; Yeginbayeva et al., 2020).

Full-scale ship trials or laboratory experiments are needed to predict the effect of surface roughness on ship hydrodynamic performance. The effect of the surface condition can be monitored through full-scale trials at clean and fouled conditions. The full-scale trials can provide high accuracy results as long as the necessities of the full-scale trials are taken into account. However, this method is not always cost-effective and practical since the ship used must be available throughout the ship trials. Moreover, other contributors affecting ship operation such as wind, wave, currents and human factors need to be considered (Townsin, 2003).

For these reasons, predicting the effect of a surface condition on ship drag strongly depends on experimental research, which needs experimental facilities. In a recent study, Yeginbayeva et al. (2018) presented an extensive review on the existing facilities used for the hydrodynamic drag characterisation of a surface which can be a freshly coated panel or a panel covered with artificial or real biofouling. Water tunnel flat plate boundary layer measurements, floating element force balance measurements, flat plate towing tank measurements, pipe flow, flat plate rectangular channels, rotating disks and rotating cylinders can be given as examples of existing facilities and methods primarily used in the literature.

Townsend's wall similarity hypothesis states that turbulence is independent of wall roughness and viscosity outside the roughness sublayer, which extends out approximately five roughness heights (k) from the wall at a sufficiently high Reynolds number. (Flack et al., 2005; Schultz and Flack, 2005; Townsend, 1980). Clauser (1954) and Hama (1954) stated that the surface roughness was influential only in the inner layer and caused a downward shift in the log-law region of the boundary layer, which is called Roughness Function, ΔU^+. In other words, the outer region of the boundary layer for both smooth and rough walls obey the velocity defect law. The universality of the velocity defect law is experimentally supported by Krogstadt and Antonia (1999) and Schultz and Flack (2003). The velocity defect profiles also supported the wall similarity hypothesis of Townsend (1980).

Once the roughness functions are obtained through the experimental methods given above, the drag of any object can be predicted based on a computational boundary layer code or similarity law analysis based on Townsend's wall similarity hypothesis (Demirel et al., 2019; Granville, 1958; Schultz, 2004; Townsin and Dey, 1990; Uzun et al., 2020).

The implementation of ΔU^+into the wall models of computational fluid dynamics (CFD) software provides a high-fidelity approach towards investigating the effect of any surface condition on the resistance of a body in question. In recent years, CFD has been widely used as a high-fidelity approach in predicting the effect of a surface condition on full-scale bodies, i.e. ships (Castro et al., 2011; Demirel et al., 2014; Farkas et al., 2018; Khor and Xiao, 2011; Song et al., 2019; Speranza et al., 2019; Uzun et al., 2021). The advantage of using CFD is that it allows capturing the change in the friction velocity, U_τ and thus the change in roughness Reynolds number, k^+over the immersed surface of a body. On the other hand, the similarity law scaling method cannot calculate the change in k^+ and accepts only one k^+ value for each section of the immersed body at a certain Reynolds number (Demirel et al., 2017).

Recently, a limited amount of work on demonstrating the use of CFD methods in predicting the effect of different surface conditions on full-scale ships has been carried out in the literature. For example, Farkas et al. (2020) investigated the impact of biofilm on the self-propulsion characteristics of the KRISO Container ship employing roughness function models within the wall function of the CFD model. The results showed that the impact of biofilm on the self-propulsion characteristics of the ship could not be ignored, with an increase in delivered power ranging from 1.4% up to 36.3%. Song et al. (2020) investigated the impact of barnacle type biofouling on the self-propulsion parameters, propulsive efficiencies and flow characteristics around the same container ship using the modified wall function approach at different fouling scenarios (i.e., fouled hull, fouled propeller and both hull and propeller fouled). The findings of the study suggest that the overall propulsive efficiency is increased for the fouled hull/clean propeller case, whereas it decreases for other cases. The increase in the delivered power was found to be 81% for the most severe condition. Mikkelsen and Walther (2020) validated their CFD simulations with the speed trial measurements for two different ships. Townsin's standard empirical formula and modified wall function method proposed by Demirel et al. (2017) were compared. The results suggest that using the modified wall function approach gives more accurate results compared to the traditional method using the empirical formula. More studies focusing on predicting the effect of surface conditions on ship resistance using CFD can be found in (Demirel et al., 2014; Song et al., 2021, Farkas et al.,2020; Farkas et al., 2021).

Hull roughness is generally defined as uniform roughness throughout the ship hull in the previous studies, whereas the biofouling accumulation on ships are completely chaotic and shows no uniformity in real conditions. Song et al., (2021a) conducted a series of towing tests using a Wigley hull with various roughness conditions i.e., smooth, full-rough, ¼-bow-rough, ¼-aft-rough, ½-bow-rough, and ½-aft-rough. The results demonstrated that roughness on the forward section of the hull is more significant among the other configurations in terms of increased frictional resistance. As a continuation study, Song et al., (2021b) performed CFD simulations for the Wigley hull with the same surface conditions in Song et al.,(2021a). The results of the CFD study showed a good correlation with the experiments. In addition, it is noted that the feature of flow around the hull showed variety based on the location of roughness. Östman et al.,(2019) conducted CFD simulations for a full-scale tanker applying two different fouling control coatings (i.e. low and high quality) at different hull locations. The results showed that this approach could reduce ship frictional resistance in a cost-effective way by using a high-quality coating where only high skin friction is concentrated. Vargas et al.,

(2019) investigated the effect of homogenous and heterogenous roughness distributions on a full-scale combatant with different roughness scenarios. The study demonstrated that the highest increase in the local skin friction is at the bow section, followed by sides, flat bottom, stern and transom.

Similar to surface ships, the effect of biofouling on submerged bodies, like a submarine, is also significant in terms of their hydrodynamic performance, particularly on their powering performance. As stated in a navy project call, coatings that may be effective when submarines are out at sea are not as effective as when the submarine is maintained in a static state for long periods. Cleaning the fouled areas requires significant diver labour with hull cleaning tools which increase maintenance cost from both manpower and radiological perspectives and reduces operational availability (Putnam, 2016). Critical design factors such as top speed, hydroacoustic stealth and acceleration are crucial for high-performance, as stated in the US Naval warship and submarine maintenance practices (ONR, 2009). Accumulation of macro fouling on ships' hull increases ship weight and drag and reduces vessel's fuel efficiency, especially for Navy ships as they move throughout the world's oceans, especially when they operate in temperate waters. Colonised barnacles and biofilms settled on the hull of a Navy ship result in roughly $1 billion annually in extra fuel costs and maintenance efforts (ONR, 2009).

The effect of biofouling roughness on the ship hydrodynamic performance has been mostly investigated for surface ships in the open literature. In contrast, submarine powering performance investigations are scarce, and it is non-existing for a full-scale submarine in the open literature under rough condition. In a recent study by Sezen et al., (2021), the scale effects on the resistance and self-propulsion characteristics were investigated using the RANS method with the k-ω SST turbulence model. In the numerical calculations, model, full-scale DARPA Sub-off forms and INSEAN E1619 propeller were used in smooth conditions. The model scale results were extrapolated to full-scale using the 1978 ITTC performance prediction method, and they were compared with those of full-scale CFD results. The numerical results showed that the 1978 ITTC performance prediction method could be reliably used for the submerged bodies (i.e., submarines) similar to surface ships. Neverthless, the numerical studies related to submarine hydrodynamics both in smooth and rough condition are still limited to model scale (e.g. Vaz et al. (2010), Chase and Carrica (2013), Sezen et al. (2018). Therefore, this study also aims to fill this research gap in the literature using a state-of-the-art CFD tool for the full-scale DARPA Suboff form.

The authors' recent study investigated the influence of uniformly distributed particular biofouling roughness on the full-scale DARPA Suboff form's resistance and nominal wake characteristics in the propeller's absence (Uzun et al., 2021). The results of this study pointed out that the presence of roughness increased the effective power ranging from ~36% to ~112%, whereas the nominal wake fraction values increased in a range from ~25% to ~68% compared to the smooth hull surface condition. However, biofouling on ships or submarines does not follow a pattern and shows no uniformity in real life. This situation can lead to mispredicted results compared to the real conditions. Therefore, it would be a beneficial attempt to investigate how heterogeneous distributed roughness on the submarine hull affect self-propulsion and powering performance compared to the fully rough (homogenous) and smooth condition.

The aim of this study is to investigate the effects of homogenous and heterogeneous distributed biofouling roughness on a full-scale submarine's powering and self-propulsion characteristics using CFD.

In this study, the flow around the model scale DARPA Suboff submarine form, which is widely used in the literature, was first solved in smooth condition. The resistance and self-propulsion characteristics of the model-scale submarine were validated with the available experimental data and other numerical studies. Following this, the resistance and self-propulsion simulations were conducted for a representative full-scale submarine based on the DARPA Suboff at a constant speed in smooth condition. The verification study was performed to determine to uncertainty level of the full-scale CFD simulations using a commercial CFD solver (StarCCM+). Furthermore, roughness functions were employed in the wall function of the CFD model, and a comprehensive set of analyses, including several roughness configurations and fouling scenarios, were performed to investigate the roughness effect on the self-propulsion characteristics of the subject submarine.

The paper is structured as follows: theoretical background, including roughness functions as well as open water and self-propulsion equations, are given in Section 2. The submarine and propeller geometry, computational domain and boundary conditions, grid structure, test matrix, as well as solution methodology are presented in Section 3. The verification and validation study is performed in Section 4. The effect of roughness on the self-propulsion characteristics are demonstrated in Section 5. Finally, conclusions are drawn, along with planned future studies in Section 6.

2 THEORETICAL BACKGROUND

2.1 *Governing Equations*

The commercial RANS solver StarCCM+, version 15.02.007 was used in order to solve the flow around the submarine hull. Details of the solver can be found in Siemens (2020). The numerical solution of the Navier-Stokes partial differential equations, the mathematical definition of flow motions, is based on viscous solvers. The finite volume approximation is used to solve this set of non-linear partial differential equations within the capabilities of StarCCM+. The governing equations can be written in generalised tensor form, respectively, as follows.

$$\frac{\partial(\rho\bar{u}_i)}{\partial x_i} = 0 \tag{1}$$

$$\frac{\partial(\rho\bar{u}_i)}{\partial t} + \frac{\partial\left(\rho\bar{u}_i\bar{u}_j + \rho\overline{u_i'u_j'}\right)}{\partial x_j} = -\frac{\partial\bar{p}}{\partial x_i} + \frac{\partial\bar{\tau}_{ij}}{\partial x_j} \tag{2}$$

Here, $\rho\overline{u_i'u_j'}$ represents the Reynolds stresses, $\bar{u}$ is the mean velocity vector $u'$is the fluctuating velocity vector, $\bar{p}$ is the mean pressure, ρ is the density and $\bar{\tau}_{ij}$ is the mean viscous stress tensor components.

$$\bar{\tau}_{ij} = \mu\left(\frac{\partial\bar{u}_i}{\partial x_j} + \frac{\partial\bar{u}_j}{\partial x_i}\right) \tag{3}$$

where μ is dynamic viscosity.

In this study, the simulations were conducted in a steady manner since the submarine model is fully submerged, and the free surface effects are not present. Thus, the first term of the momentum equation was ignored.

2.2 *Roughness Functions and approach*

The non-dimensional velocity distribution in the log-law region for a rough surface can be described by Eq. 4.

$$U^+ = \frac{1}{\kappa}\ln(y^+) + B - \Delta U^+ \quad (4)$$

where U^+represents the non-dimensional velocity, κ represents the von Karman constant, y^+represents the non-dimensional normal distance from the boundary, B represents log law intercept. The superscript + indicates the inner variables normalised with U_τ or U_τ/v (U_τ is the friction velocity and v is the kinematic viscosity of the fluid).

Roughness causes a downward shift in the velocity profile, which is commonly shown as ΔU^+. Drag characterisation of a rough surface is to find ΔU^+ as a function of k^+ which is defined in Eq. 5. It is important to note that ΔU^+ is equal to zero for the smooth condition, whereas it needs to be obtained experimentally for the rough condition.

$$k^+ = \frac{kU_\tau}{v} \quad (5)$$

k represents the roughness length scale.

Roughness functions provided in Uzun et al. (2020) were used to investigate barnacle type biofouling's effect on the submarine's self-propulsion characteristics. Uzun et al. (2020) conducted an extensive series of towing tank tests of flat plates covered with 3D printed artificial barnacle tiles varying in barnacle sizes, coverage areas and settlement patterns. Roughness functions were then calculated based on the overall method, and full-scale predictions were made using boundary layer similarity law analysis. It is of note that the roughness functions and corresponding roughness Reynolds heights show an excellent agreement with the Colebrook type roughness function of Grigson (1992), described by Eq.6. Table 1 tabulates the roughness length scales of the rough surfaces used in this study.

$$\Delta U^+ = \frac{1}{\kappa}\ln\,(1 + k^+) \quad (6)$$

Table 1 Roughness length scales of test surfaces, adapted from Uzun et al. (2020).

Test Surfaces	Surface Coverage (%)	Barnacle Height *h* (mm)	Roughness length scale k_G (μm)	Equivalent sand roughness height *ks* (μm)
Mix	10	5, 2.5, 1.25	94	409
NS Mix	10	5, 2.5, 1.25	136	635
Mix	20	5, 2.5, 1.25	337	1366
NS Mix	20	5, 2.5, 1.25	408	1645

2.3 *Open water and self-propulsion characteristics*

The non-dimensional thrust, K_T and torque K_Q, advance coefficient, J and open water efficiency are calculated as follows:

$$K_T = \frac{T}{\rho n^2 D^4} \tag{7}$$

$$K_Q = \frac{Q}{\rho n^2 D^5} \tag{8}$$

where, T represent the propeller thrust, ρ is the density, Q is the propeller torque, n is the propeller rotational speed, and D is the propeller diameter. Advance coefficient, J can be shown as:

$$J = \frac{V_a}{nD} \tag{9}$$

where V_a is the average incoming velocity at the propeller plane. Advance coefficient, J is calculated by equalising the thrust at self-propulsion with the thrust of open water based on the thrust identity method. The open water efficiency and the delivered power, P_D to the propeller are calculated as below:

$$\eta_O = \frac{JK_T}{2\pi K_Q} \tag{10}$$

$$P_D = 2\pi nQ \tag{11}$$

If the propeller is advancing in open water at the same J, the open water torque coefficient, K_{Q_O}would be different from that measured behind the ship model. This ratio $K_{Q_O}/K_{Q_b}$is known as the relative rotative efficiency, η_R:

$$\eta_R = \frac{K_{Q_O}}{K_{Q_b}} = \frac{\eta_B}{\eta_O} \tag{12}$$

where η_B is the propeller efficiency behind the hull.

Other self-propulsion characteristics including thrust deduction fraction, t, wake fraction, w, hull efficiency, $\eta_H$and propulsive efficiency, η_D, defined as follows, where R_T represents the total resistance in the absence of a propeller.

$$t = 1 - \frac{R_T}{T} \tag{13}$$

Wake fraction (w) is computed based on thrust identity as follows:

$$w = 1 - \frac{JDn}{V_s} \tag{14}$$

where V_s is the ship speed. As mean wake fraction and thrust deduction are known, hull efficiency can be calculated as follows:

$$\eta_H = \frac{1-t}{1-w} \tag{15}$$

The propulsive efficiency, η_D is defined as

$$\eta_D = \eta_O \eta_R \eta_H \tag{16}$$

3 GEOMETRY AND TEST MATRIX

3.1 *Submarine and propeller geometry*

Defence Advanced Research Projects Agency (DARPA) designed a benchmark submarine model with two different configurations, namely AFF-1 and AFF-8. The discrepancy between the configurations is that the AFF-8 has appendages such as rudders and sails at the end and the bow sections of the hull, as shown in Figure 1, whereas AFF-1 has no appendages (bare form). The AFF-8 was selected to be used in the simulations for understanding the effect of biofouling on the self-propulsion characteristics of a scaled-up representative full-scale submarine for a scale ratio, λ=24. Table 2 tabulates the main geometrical properties of the submarine form. Detailed information about the submarine geometry can be found in Groves et al., (1989). The benchmark INSEAN E1619 propeller was used to propeller the DARPA based submarine in the simulations. The 3D view of the representative submarine hull and its propeller are shown in Figure 1. The main particulars of the propeller are tabulated in Table 3.

Table 2 The main properties of the DARPA Suboff Form (Groves et al., 1989)

		AFF-8 (Model Scale, λ =24)	**AFF-8 (Full Scale, λ =1)**
Length overall	**L_{OA} (m)**	4.356	104.5
Length between perpendiculars	**L_{BP} (m)**	4.261	102.3
Maximum depth	**D_{max} (m)**	0.508	12.2
Wetted surface area	**S (m^2)**	6.348	3656.4
Displacement volume	**∇ (m^3)**	0.706	9759.7

Table 3 Main particulars of E1619 propeller

Main Particular	Symbol	Model	Full
Scale	λ	24	1
Diameter	D (m)	0.262	6.288
Pitch to diameter ratio	P/D	1.15	1.15
Number of blades	Z	7	7
Hub to diameter ratio	D_h/D	0.226	0.226
Expanded blade area ratio	A_E/A_0	0.608	0.608
Rotational direction	-	Right hand	Right hand

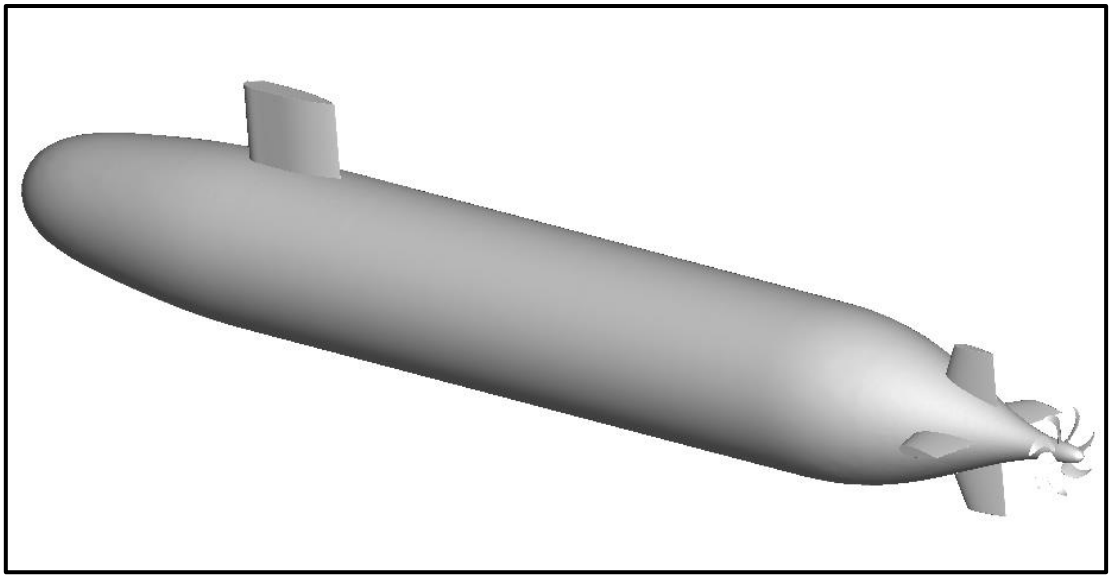

Figure 1 3D view of DARPA Suboff hull form and INSEAN E1619 propeller.

3.2 *Computational Domain and Grid Structure*

The computational domain and the selected boundary conditions for the self-propulsion simulations are illustrated in Figure 2. The domain has two regions, including a stationary region for the submarine hull and a rotating region for the propeller. The applied boundary conditions for the simulations are the pressure outlet for the outlet boundary located at the positive *x*-direction and the velocity inlet for the inlet boundary at the negative side of the *x*-axes. Other boundaries are set to symmetry planes. The no-slip wall boundary condition is applied for the submarine hull, propeller blades and appendages. The outlet boundary is located at a $5L_{BP}$ distance from the aft perpendicular of the submarine, whereas the inlet is located at a $1.5L_{BP}$ distance from the forward perpendicular of the submarine. The top and bottom symmetry planes are located at a $2L_{BP}$ distance from the centre of the submarine hull.

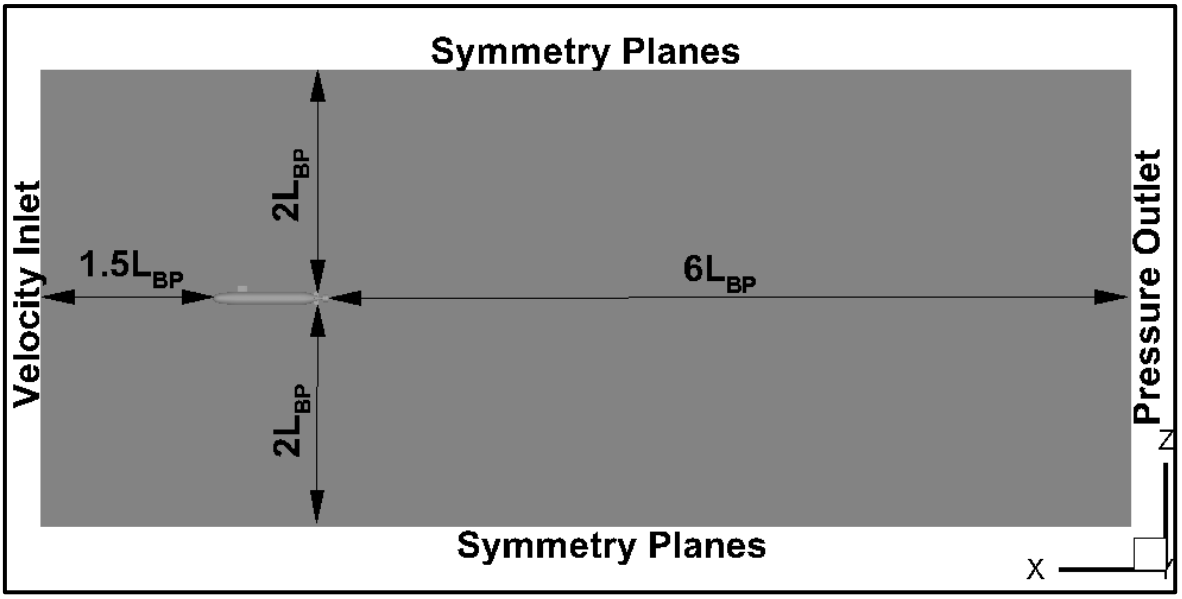

Figure 2 The representation of the computational domain and boundary conditions for the self-propulsion simulations

The generation of a sufficient grid structure is one of the critical steps for most hydrodynamic applications, which may cause discretisation errors in the numerical solvers. The meshing tool of STAR-CCM+ was used to generate a region-based mesh to discretise the computational domain with the finite volume method. Trimmer mesh with the hexahedral elements is used to obtain an accurate solution. Local mesh refinements are applied in the regions where adverse pressure gradients and flow separations likely occur. The unstructured mesh and local refinements can be seen in Figure 3.

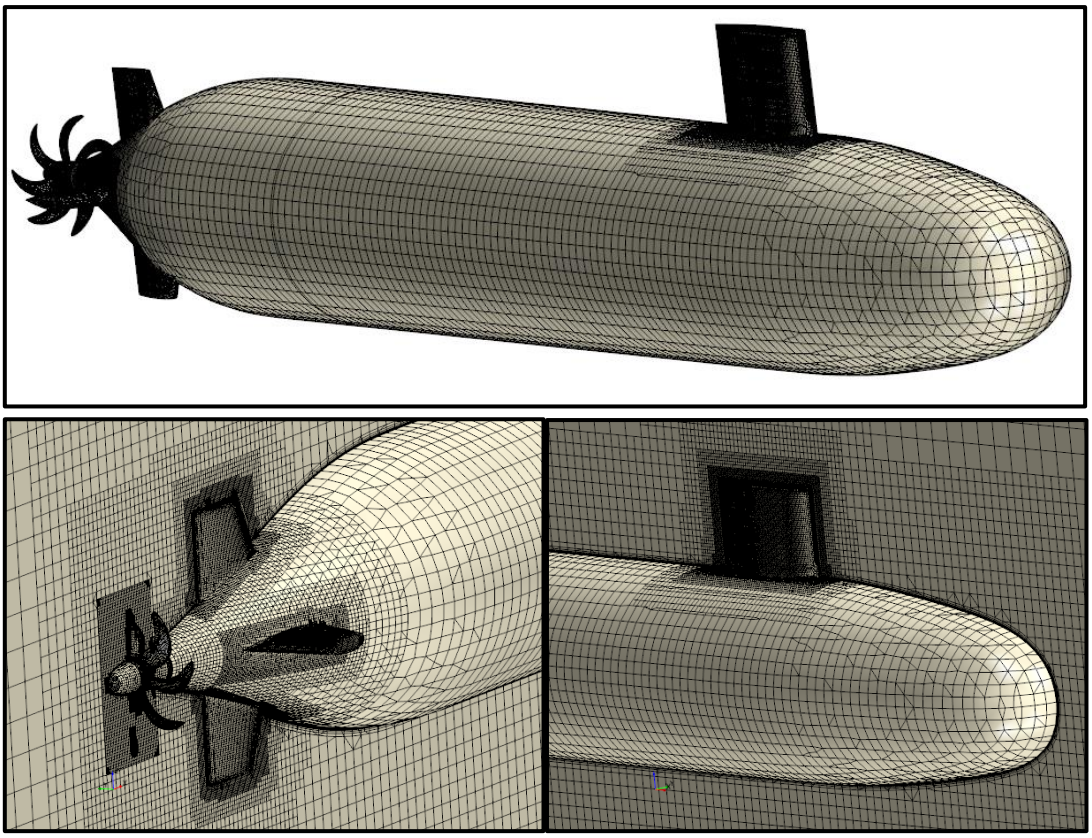

Figure 3 Unstructured grid around the full-scale submarine form

3.3 *Test Matrix*

The effect of barnacle type biofouling on the self-propulsion characteristics was investigated through five different fouling scenarios, as given in Table 4. The forward speed of the submarine was selected as 20 knots for the self-propulsion simulations. The submarine hull was divided into three equal sections in terms of its wetted surface area to predict the effects of heterogeneous roughness distribution on the self-propulsion characteristics of the submarine. The fouling scenarios are also shown in Figure 4. The black regions show the roughness application area on the submarine hull.

Table 4 Fouling scenarios and surface conditions

Fouling scenarios	Fouling distribution	Surface condition
C0	Full body	Smooth
C1	Full body	Mix10, Mix20, NSMix10, NSMix20
C2	Forward-section	Mix10, Mix20, NSMix10, NSMix20
C3	Mid-section	Mix10, Mix20, NSMix10, NSMix20
C4	Aft-section	Mix10, Mix20, NSMix10, NSMix20

As seen in Table 4, four different surface conditions were selected for the fouling scenarios. Therefore, in total, 17 simulations were conducted in this study. It is important to note that roughness is only distributed to the submarine hull surface as the effect of surface roughness on the propeller has no significant effect on self-propulsion characteristics (Song et al., 2020) (Farkas et al., 2020), while the effect of roughness may be important for cavitation inception and its consequence which is beyond the scope of the current investigation. Thus, the propeller surface was assumed clean in the scope of this study.

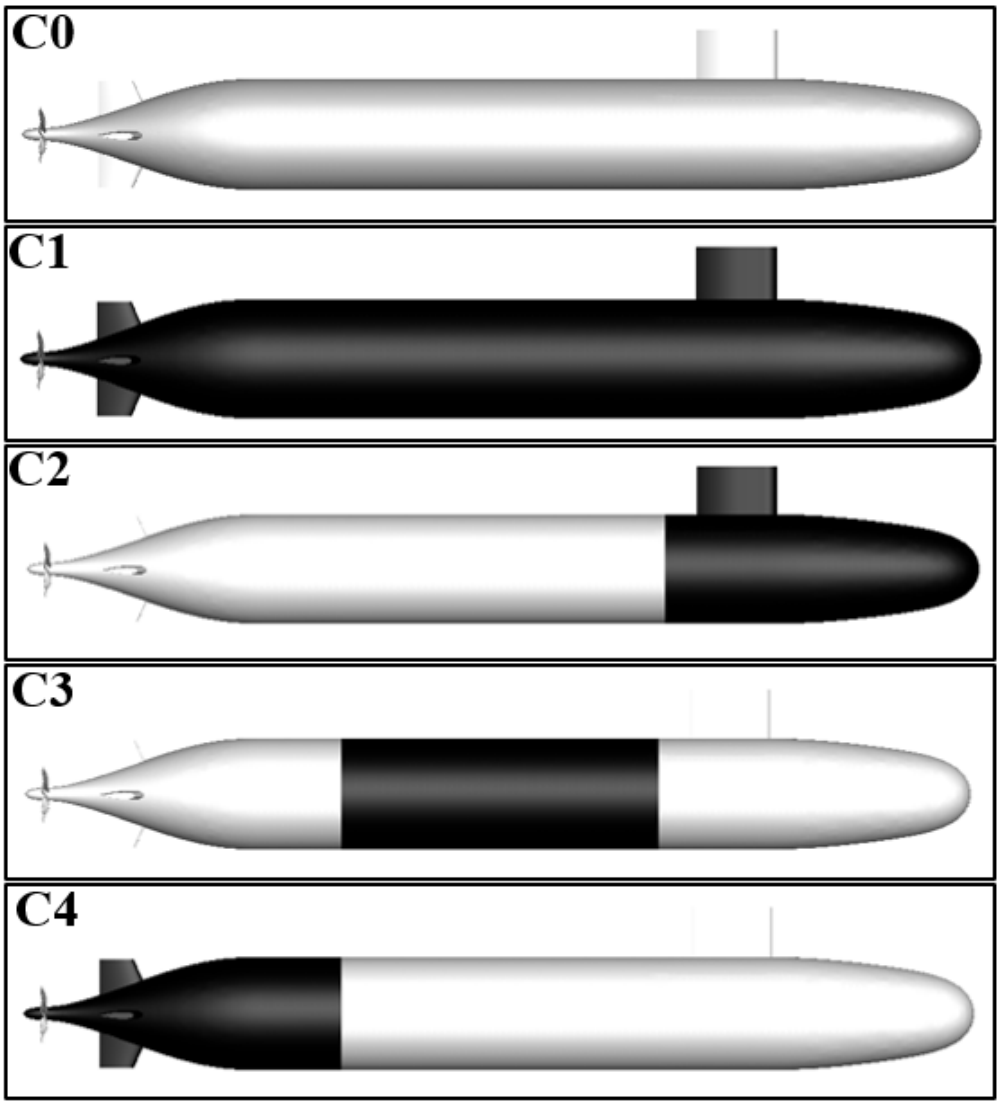

Figure 4 The representation of roughness application area on the hull surface, black colour represents the roughness application area.

3.4 *Solution Methodology*

The commercial CFD tool, Star CCM+, was used for numerical computations. In this study, the steady RANS solver was used together with the shear stress transport (SST) k-ω turbulence model. The reason for using the SST k-ω turbulence model is that this model uses the standard k- ω model in the near-wall region and gradually makes a transition into the standard k-ε model away from the wall (Menter, 1994). In this way, the free stream sensitivity problem of the standard k-ω model is eliminated without compromising the near-wall performance of the k-ω model. The model is successful at solving the boundary layer flows under the adverse pressure gradient and separation points. Governing equations were solved in a segregated manner, and discretisation was made through the second-order upwind convection scheme to increase the solution's accuracy.

The all y^+ formulation was selected to switch automatically between low and high Reynolds wall models for the flow fields with a different boundary layer thickness (hull of the submarine and its appendages). The continuity and momentum equations were linked via a predictor-corrector SIMPLE-type algorithm. Since the blending/switching behaviour is inaccurate for the

wall function approach in the buffer layer region (5<y^+<30), y^+ values were selected such that y^+ values are always higher than 30 to prevent numerical errors. Moreover, y^+should also be higher than k^+values as recommended by Star CCM+. The first grid node distance from the wall must exceed the roughness height in question; otherwise, the skin friction coefficient is under-predicted. The y^+ distribution on the submarine hull surface in smooth condition can be seen in Figure 5. As shown in Figure 5, the averaged y^+ value computed is 410 both for the submarine hull and its propeller.

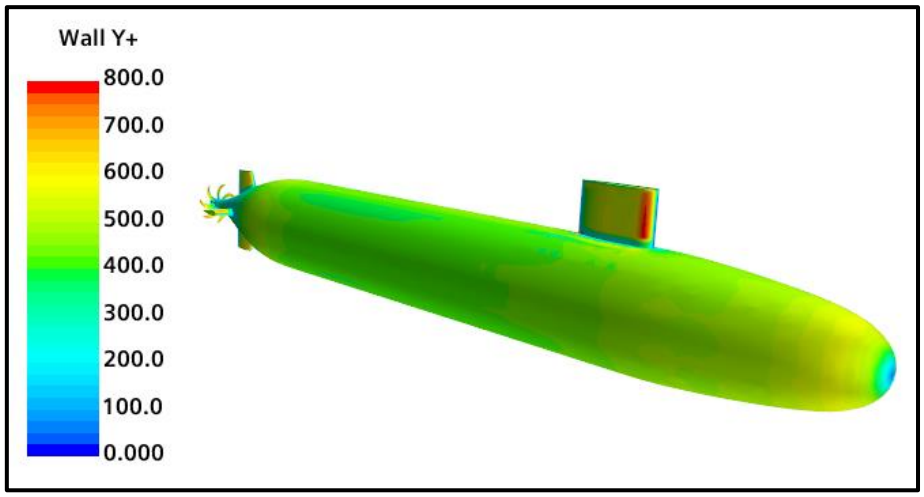

Figure 5 The y^+ distribution on the hull and propeller in full-scale

The Moving Reference Frame (MRF) approach was used to model the rotational motion of the propeller. The MRF approach provides a steady approximation, and it is a cost-wise approach in terms of the computational cost compared to the sliding mesh technique. However, the MRF approach may not be as accurate as of the sliding mesh technique, particularly for unsteady simulations. The discretised propeller was used to model the hull-propeller interaction. The self-propulsion characteristics were calculated based on the thrust identity method at the self-propulsion point using the experimental open water data for the selected propeller.

3.5 *Propeller controller*

The self-propulsion point needs to be obtained for the propulsion test by towing the model at a target speed and adjusting the propeller rotation speed to balance the thrust and hull resistance (Carrica et al., 2010) (ITTC, 2002). The drawback of this approach, while following it in the CFD method, is the determination of the self-propulsion point in a cost-effective manner as this requires several runs at different propeller rotational speeds, which lead to increased computational costs. A proportional-integral (PI) controller can be used to prevent the increased costs by controlling the propeller speed and finding the self-propulsion point efficiently.

The general formulation of the controller can be expressed as follows.

$$n(t) = n_0\left(1 + K_p \cdot error + K_i \sum error\right) \tag{17}$$

where, n_0 is the initial propeller rotational speed, rps; t is the time, s. K_i and K_p are the gain for the integral and proportional gains of the PI controller, respectively. The error is defined as the difference between total resistance (R_T) and propeller thrust (T) with the following formulation.

$$error = R_T - T \tag{18}$$

It should be noted that the selection of the K_i and K_p is critical in terms of the stability and convergence rate of the PI controller. The optimum K_i and K_p values can be found after several trial and errors to increase the convergence speed of the simulation. In this study, the K_i and K_p values were set to 10^{-5} for both model and full-scale.

4 VERIFICATION AND VALIDATION

4.1 *Verification study*

A verification study is performed using the Grid Convergence Index (GCI) method based on the Richardson extrapolation to estimate the numerical uncertainties of the simulations. It is of note that the uncertainty method (i.e., GCI) recommended by the ITTC procedures (ITTC, 2011) is used in CFD verifications. This method was first proposed by Roache (1997) and has been employed in many studies in the literature. The methodology followed in this study was described by Celik et al. (2008), in which the details of the procedure can be found.

The refinement factor (r) was selected as $2^{0.5}$, which is generally employed in CFD applications. Besides, it is recommended to use a refinement factor greater than 1.3. It should be noted that the three different solutions are required to make an accurate assessment for the uncertainty of the numerical solution (Roache, 1998). Therefore, three different solutions were implemented in this study. In the uncertainty study, the solution scalar was selected a non-dimensional total resistance coefficient in the self-propelled condition at V_S=20 knots.

The difference between the solution scalars (ε) can be found using the following equation,

$$\varepsilon_{21} = \varphi_2 - \varphi_1, \quad \varepsilon_{32} = \varphi_3 - \varphi_2, \tag{19}$$

where, φ_1, φ_2, φ_3 represents the fine, medium and coarse grid solution, respectively. The total element counts of fine medium and coarse grid structures for the simulations are given in Table 5.

Convergence conditions of the numerical solution can be calculated as follows,

$$R = \frac{\varepsilon_{21}}{\varepsilon_{32}} \tag{20}$$

The determination of the solution can be assessed according to the range of R value (Stern et al., 2006). Oscillatory convergence: -1 < R < 0, monotonic convergence: 0 < R < 1, oscillatory divergence: R < -1 and monotonic divergence: R > 1.

The extrapolated value can be calculated using the following equation,

$$\varphi_{ext}{}^{21} = (r^p \varphi_1 - \varphi_2)/(r^p - 1) \tag{21}$$

The approximate and extrapolated relative errors are defined as follows,

$$e_a{}^{21} = \left|\frac{\varphi_1 - \varphi_2}{\varphi_1}\right| \quad e_{ext}{}^{21} = \frac{|\varphi_{ext}{}^{12} - \varphi_1|}{\varphi_{ext}{}^{12}} \tag{22}$$

Finally, the uncertainty level of the numerical solution can be calculated by,

$$GCI_{fine}{}^{21} = \frac{1.25 e_a{}^{21}}{r_{21}{}^{p} - 1} \tag{23}$$

Here p is the apparent order of the method. Table 6 tabulates the element count and solution of the scalars for each grid structure and the uncertainty level of the numerical study for the full-scale simulations. It is of note that the verification study for the model scale submarine form can be found in our recent study (Uzun et al., 2021).

Table 5 Grid type and total cell numbers for simulations

Grid type	Total number of cells (Hull+Propeller)
Fine	2.710x10^3
Medium	1.679 x10^3
Coarse	1.091 x10^3

Table 6 Spatial Converge study results (V_S =20 knots)

φ_1	2.38x10^{-3}
φ_2	2.40*10^{-3}
φ_3	2.51*10^{-3}
r_{21}	1.17
r_{32}	1.15
ε_{21}	1.84*10^{-5}
ε_{32}	1.11*10^{-4}
p	11.38
q	0.11
s	1
$e_a{}^{21}$	7.72*10^{-3}
$e_{ext}{}^{21}$	1.50*10^{-3}
$\varphi_{ext}{}^{21}$	2.38*10^{-3}
GCI_{FINE} (%)	0.19

As a result of the verification study, the uncertainty of the numerical solution was calculated to be 0.19%. Hence, the fine grid resolution was selected for all simulations. It is important to note that the same near-wall mesh properties were used for each roughness configuration.

4.2 *Validation Study*

The total resistance of the model scale submarine form (i.e., λ=24) was validated with the available experimental data (Liu and Huang, 1998). Figure 6 shows that there is a good agreement between the CFD prediction and the experimental measurement. The absolute relative difference between the CFD prediction and the experimental values was found a maximum of 7% for the total resistance.

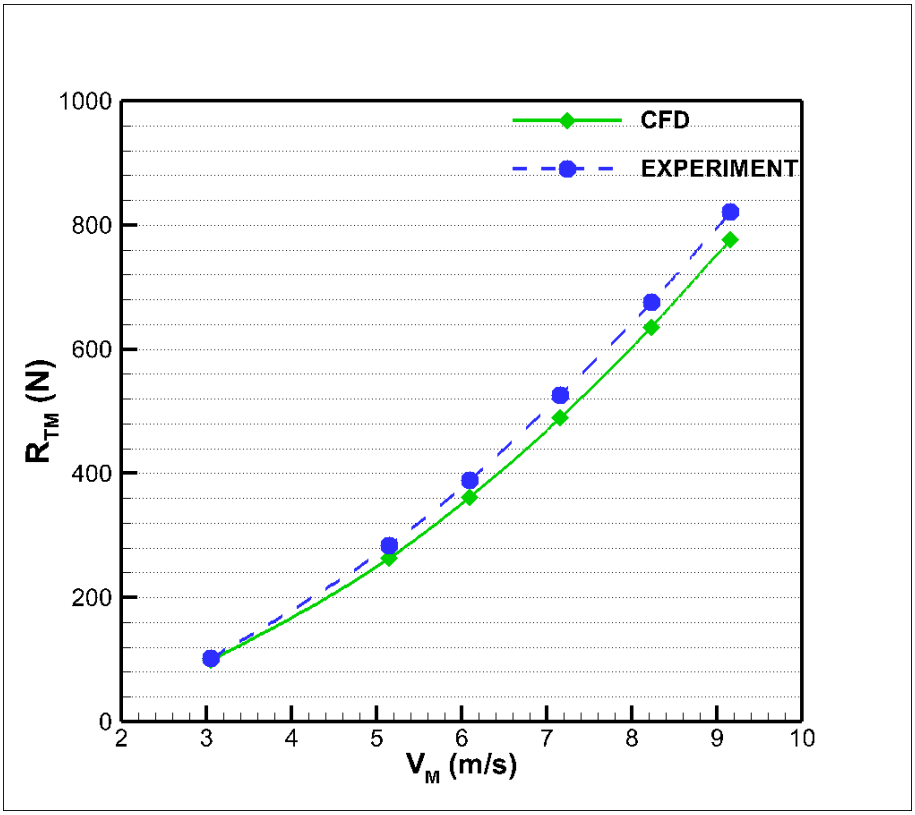

Figure 6 Validation of total resistance for the model scale submarine form (λ=24)

The self-propulsion results are compared with the other numerical studies in the literature for the model of submarine form (λ=24) at V_M=2.75 m/s in Table 7. As shown in Table 7, the present results are found to be similar to those of other numerical studies using the same propeller conducted with different numerical solvers in the literature.

Table 7 Comparison of propeller characteristics in the self-propelled case at $\mathbf{V_M}$=2.75 m/s and $\boldsymbol{\lambda}$=24

Numerical Studies (Self-Propelled Case)	K_T	K_Q
Chase and Carrica (2013), CFD	0.2342	0.0471
Kinaci et al. (2018), CFD	0.2312	-
Ozden et al. (2019), CFD	0.2416	0.0464
Ozden et al. (2019), EFD	0.2751	0.0561
Sezen et al. (2018), CFD	0.2363	0.0456
Present study	0.2342	0.0452

5 NUMERICAL RESULTS

The effect of barnacle type biofouling on the self-propulsion characteristics of a full-scale submarine hull was investigated through 17 different configurations at 20 knots of the submarine forward speed, as tabulated in Table 4. Open-water and resistance characteristics, used to evaluate the self-propulsion factors, are obtained from Uzun et al., (2021) and Sezen et al., (2021). The results are also tabulated in the appendix Table A1-A8.

Figure 7 shows the change in total resistance coefficients, C_T at the self-propulsion point with a change in roughness length scale. The C_T values are plotted against roughness length scales of the surface condition, as shown in Table 1. It is important to note that, C0 configuration represents the smooth condition, which can be considered the reference condition. The figure pinpoints that the C1 condition, which is homogenous barnacle biofouling covering the whole submarine hull surface, showed the highest increase in the C_T values compared to C0 (smooth self-propulsion) condition, as expected.

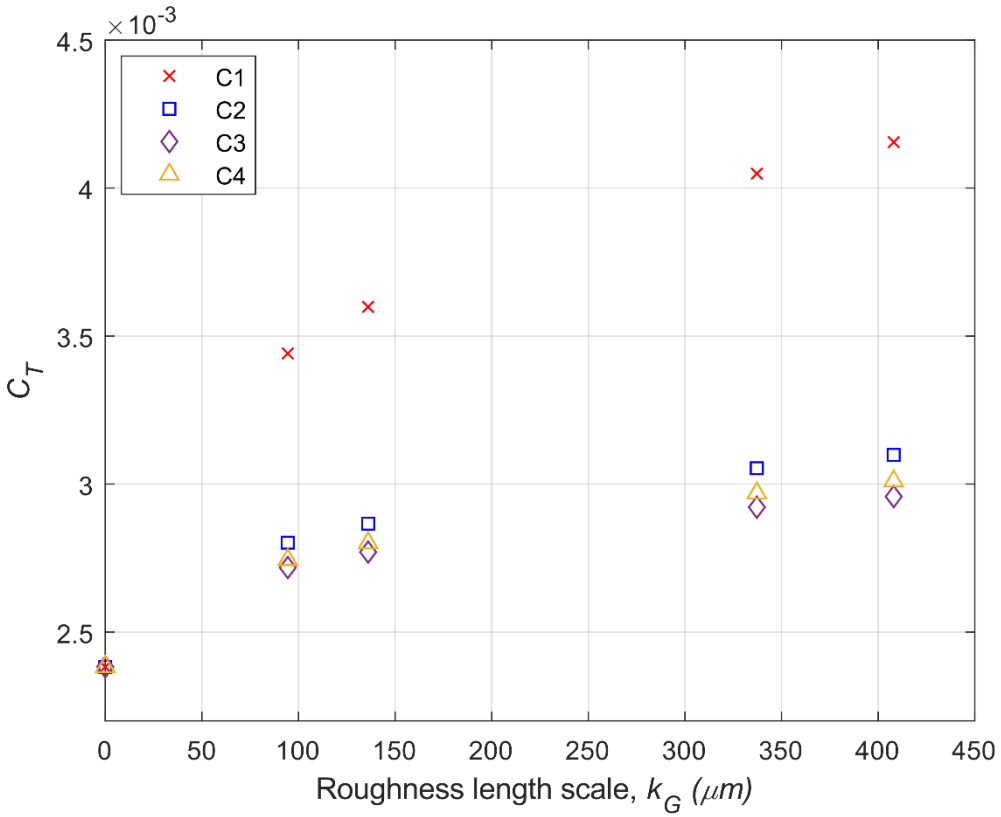

Figure 7 Total resistance coefficient, $\boldsymbol{C_T}$ at self-propulsion point against roughness length scales of surface conditions.

The increases in C_T values followed by C2, C4 and C3 configurations, respectively. Figure 7 demonstrates that the resistance penalty due to the hull roughness on the forward section of more pronounced than those on the mid and aft sections. This can be attributed to the fact that the effect of roughness can be more dominant at the points where the boundary layer is thin, and the flow experiences more dramatic speed and pressure changes as a result of the hull form change and resulting separation. This concurs well with the previous findings of conducted studies for ships, which states that hull roughness of the front part of the ship results in more added resistance than the hull roughness in other regions.

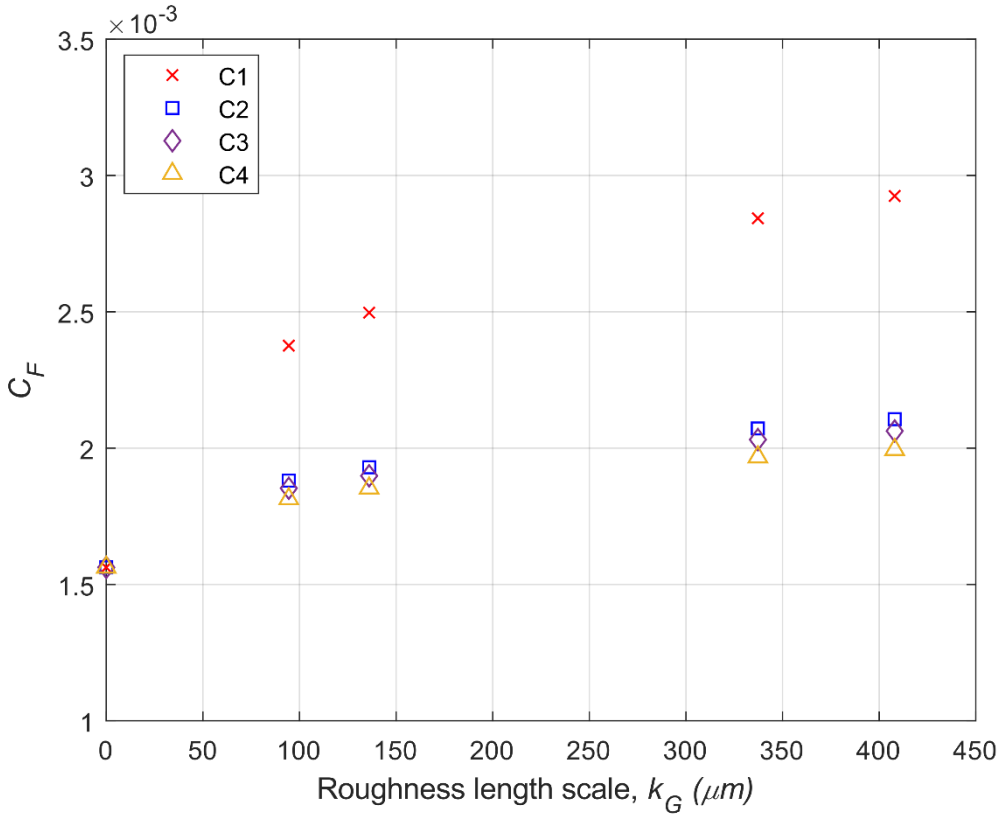

Figure 8 Frictional resistance coefficient, $\boldsymbol{C_F}$ at self-propulsion point against roughness length scales of surface conditions

Figure 8 illustrates the increases in the frictional resistance coefficients, C_F values for the different roughness configurations. It is evident that the highest increase in C_F occurred in the C1 configuration, as expected. However, unlike the discrepancies in C_T values, C_F values of the configurations are close to each other. The increases in the, C_F values due to roughness can be listed as C2, C3 and C4 from highest to lowest increase.

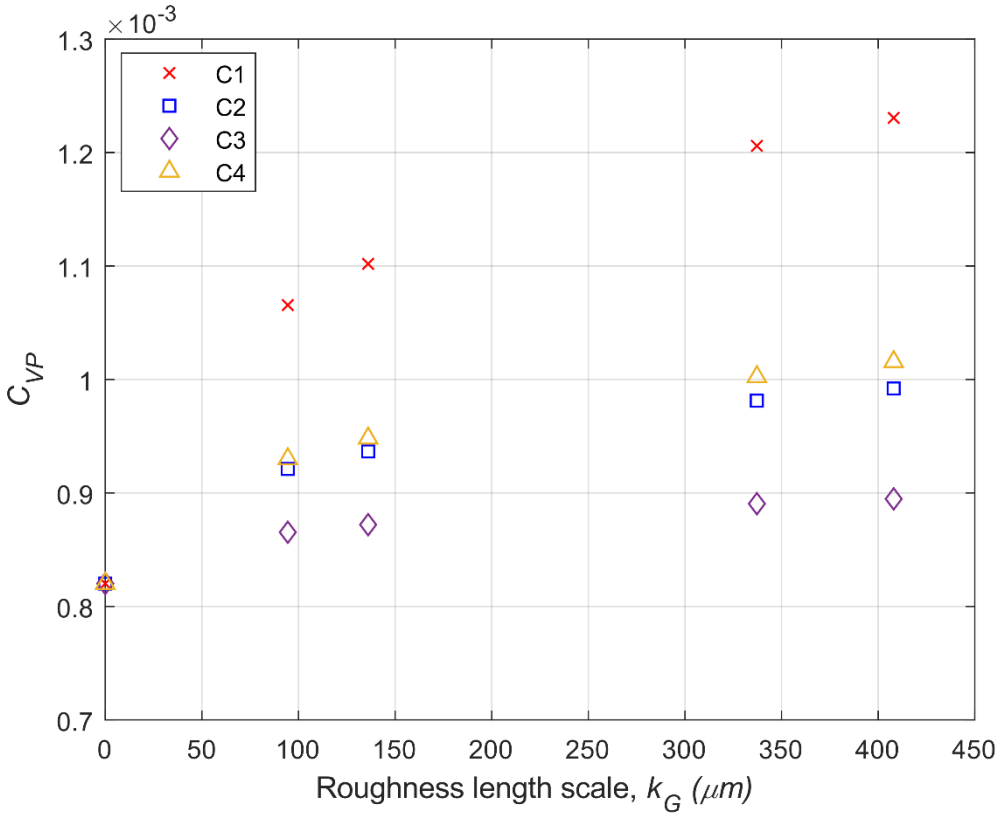

Figure 9 Pressure resistance coefficient, $\boldsymbol{C_P}$ at self-propulsion point against roughness length scales of surface conditions

Although heterogeneous roughness distribution does not show significant differences in the C_F values, the changes in the viscous pressure coefficient, C_{VP} are more discernible, especially for the C3, as shown in Figure 9. This can be explained by that the roughness increases the flow pressure dominantly where the flow is disturbed due to the form of the body as in C4 and C2, whereas the increase remains limited in C3 in which the roughness is distributed only over the parallel body (where no significant pressure change occurs). It is of note that the common point from the figures is that the differences between the C_{VP} values of the C2, C3 and C4 rise with the increasing roughness length scales.

Figure 10 shows the self-propulsion points in terms of the shaft speed, n, under varying roughness conditions. The results state that there is an increasing trend in the n values with increasing roughness length scales. As expected, the increase in resistance values causes an increase in the shaft speed with the roughness to balance the thrust and resistance values

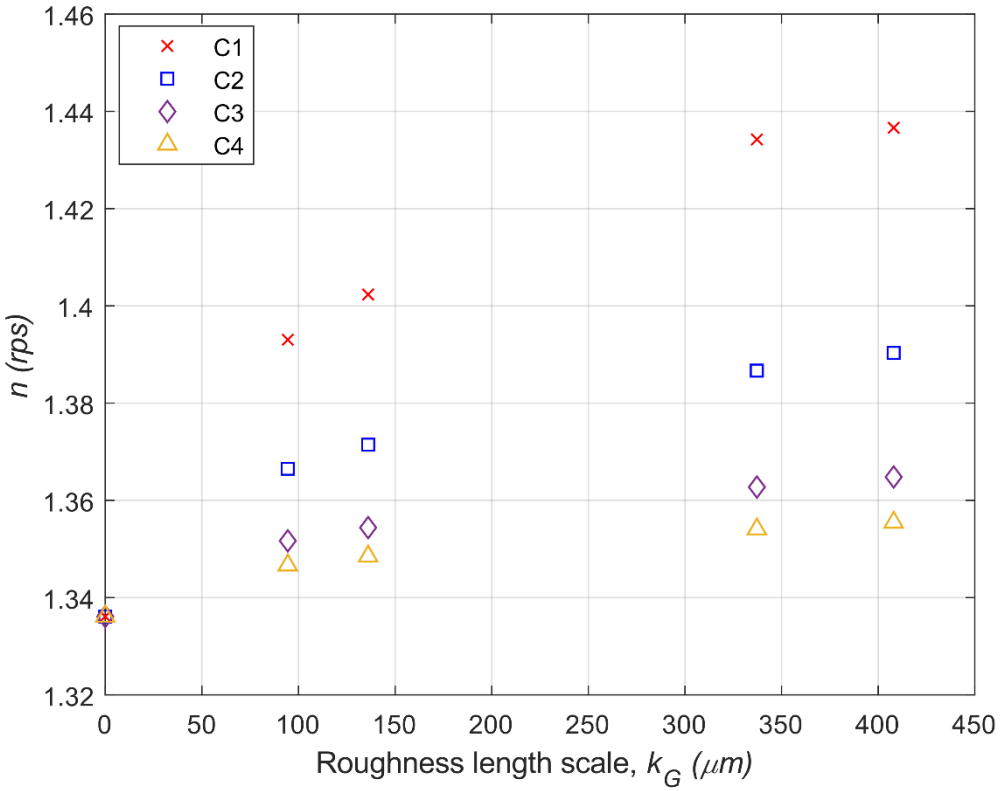

Figure 10 Rotational speed of the propeller (shaft speed), $\boldsymbol{n}$ at self-propulsion point against roughness length scales of surface conditions

It can be seen from Table A1-A4, both K_T and K_Q increase due to the presence of barnacle type biofouling compared to the smooth condition. It is evident that the changes in the K_T and K_Q values increase as the roughness length scale increases. As expected, the highest increases occurred in the K_T and K_Q values of the C1 condition with the increases varying from 32.87% to 50.84% and from 21.55% to 32.52%, respectively.

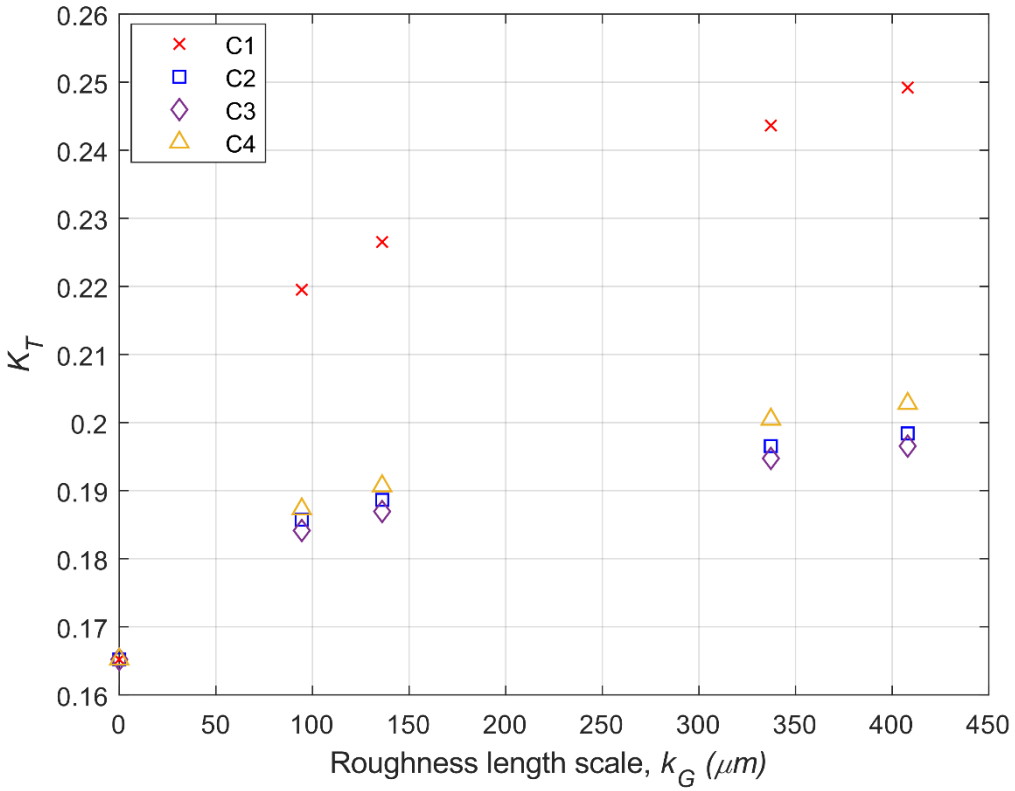

Figure 11 Thrust coefficient, $\boldsymbol{K_T}$ at self-propulsion point against roughness length scales of surface conditions

It has been observed from Figure 11 and Figure 12 that there is no significant difference in the K_T and K_Q values due to heterogeneous roughness distribution. As shown in Table A1-A4, the increases in the K_T and $K_Q$values for C4 are slightly higher than those in C2 and C3. The results state that the roughness occurrence at the aft section of the hull has slightly more pronounced effects on the K_T and $K_Q$values.

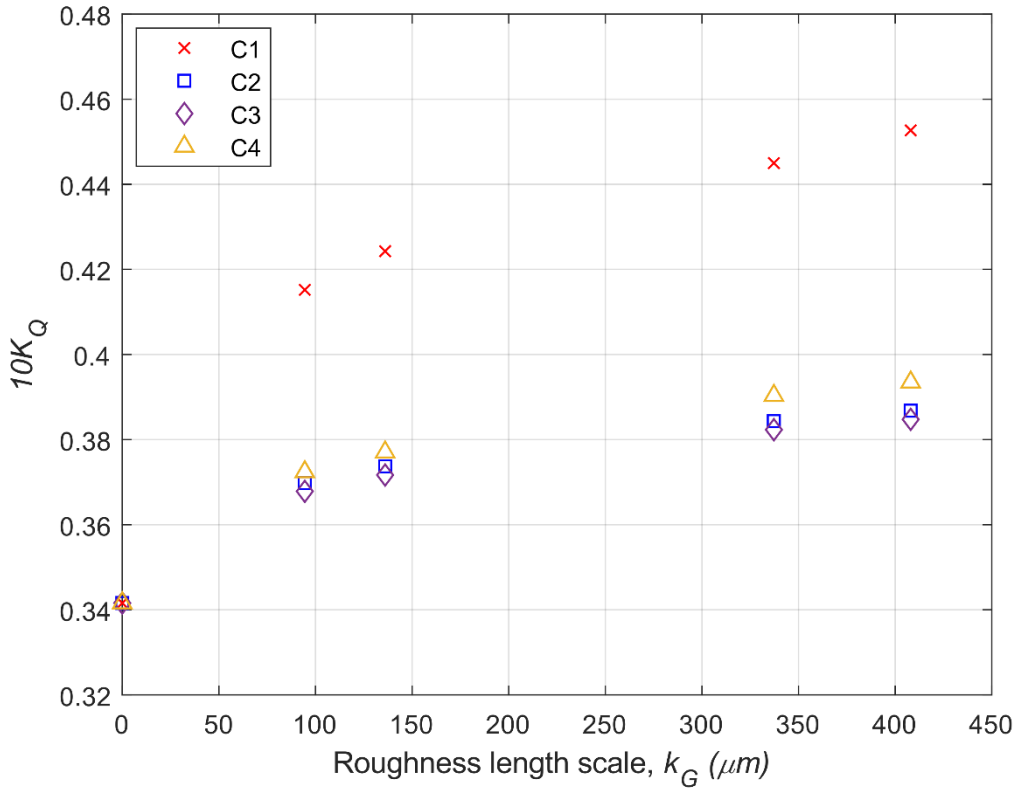

Figure 12 Torque coefficient, $10\boldsymbol{K_Q}$ at self-propulsion point against roughness length scales of surface conditions

Figure 13 illustrates the change in the J values in the presence of biofouling type roughness. As seen in the figure, there is a general decreasing trend in the J values with an increase in the roughness length scale. This is simply because of the decreasing V_a (speed of advance) values and increasing n values due to the presence of roughness around the submarine hull. The decrease in the V_a values can also be attributed to the expanding wake-field w, which in return causes a slower flow around the propeller due to roughness. The effect of heterogeneous roughness distribution over the hull did not show the discernible difference in J values similarly to K_T and K_Q.

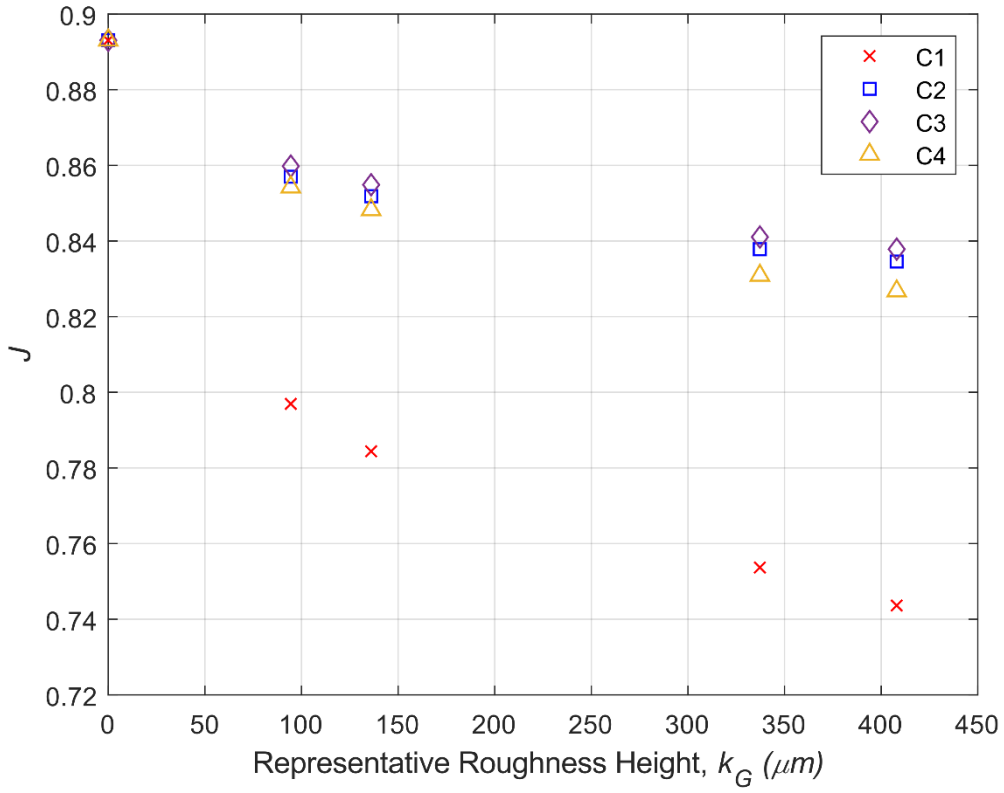

Figure 13 Advance coefficient, ***J*** at self-propulsion point against roughness length scales of surface conditions

Figure 14 compares the changes in the propeller efficiency, η_O, values under the effect of increasing roughness length scales. As seen from the figure, the highest decrease is observed in the η_O values of the C1 configuration with a decrease varying from -1.52% to -3.95%. No significant difference revealed between the heterogeneous configurations. The change in the η_O values of C2, C3 and C4 configurations were up to -0.59% compared to the smooth condition.

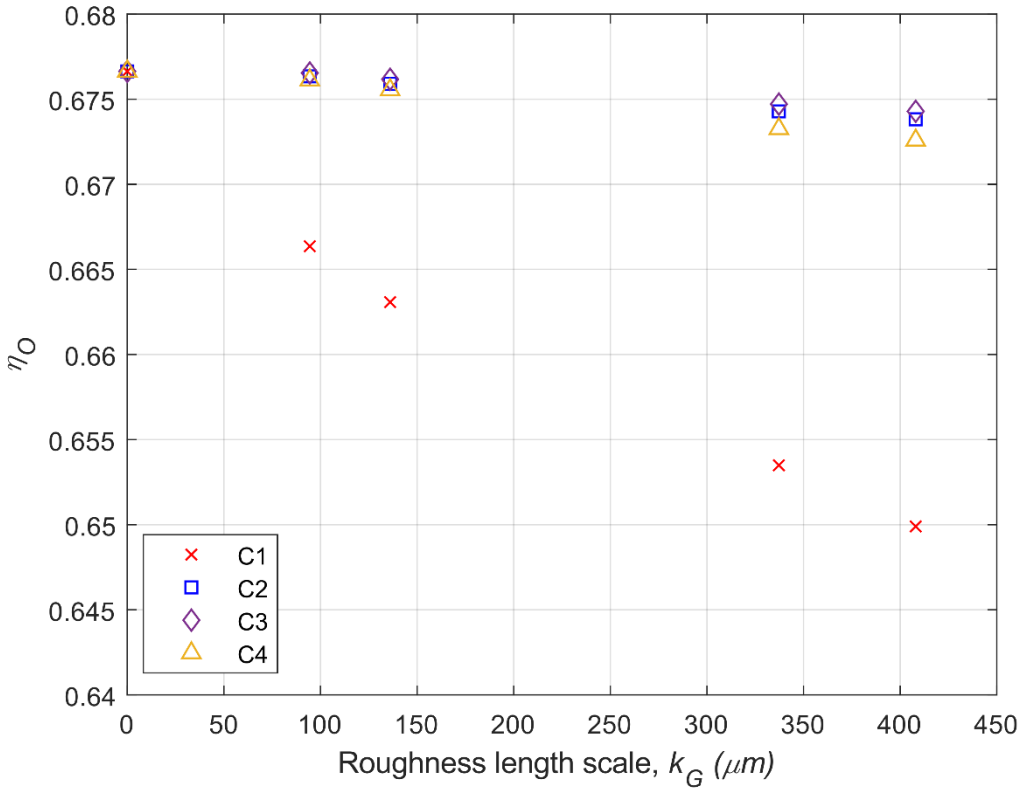

Figure 14 Propeller efficiency, $\boldsymbol{\eta_O}$ at self-propulsion point against roughness length scales of surface conditions

Propellers are set to work at an ideal J value which corresponds to the ideal η_O value. For this reason, a decrease in the J is undesirable and causes a decrease in the optimum η_O. The decrease in η_O ranges from -0.01% for C3 up to -3.95% for C1.

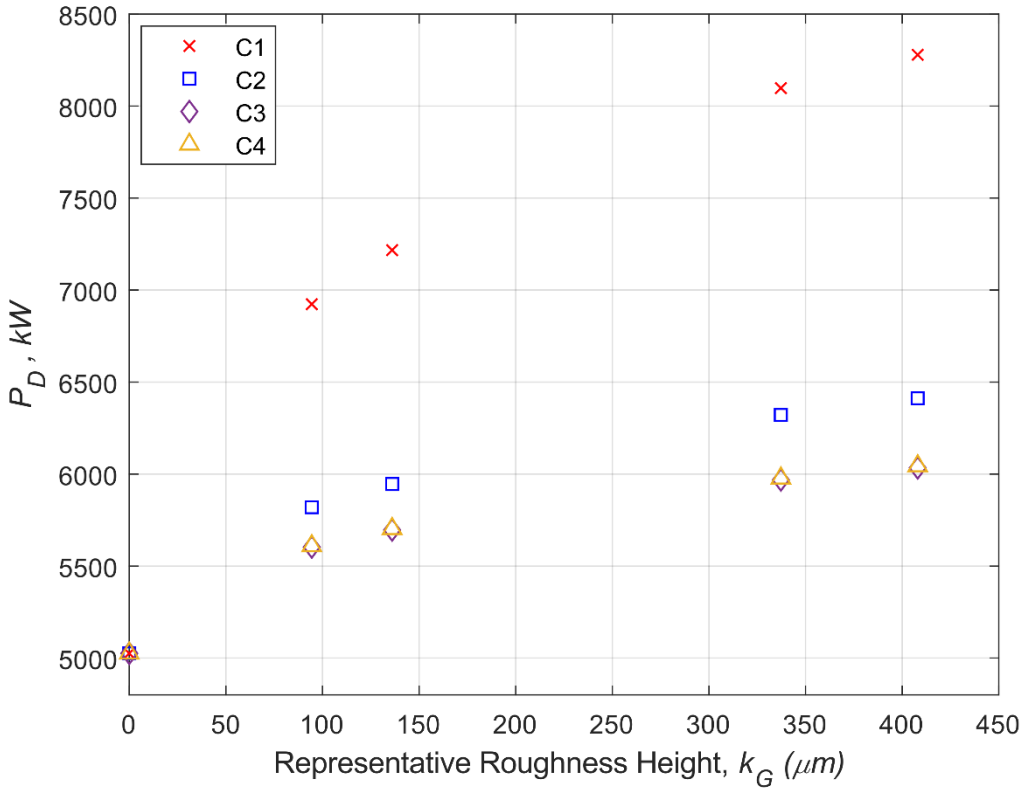

Figure 15 Delivered power to the propeller, $\boldsymbol{P_D}$ at self-propulsion point against roughness length scales of surface conditions

The effect of surface roughness on the delivered power, P_D, is critical, which causes an increase in P_D from 11.49% for C3 up to 64.73% for C1, as jointly shown in Figure 15 and Table A1-A4. This increase can be explained by the effect of roughness on the hull resistance and self-propulsion characteristics. The change in the R_T was predicted to be in a range from 14.42% for C3 up to 76.21% for C1, as given in Table A1-A4.

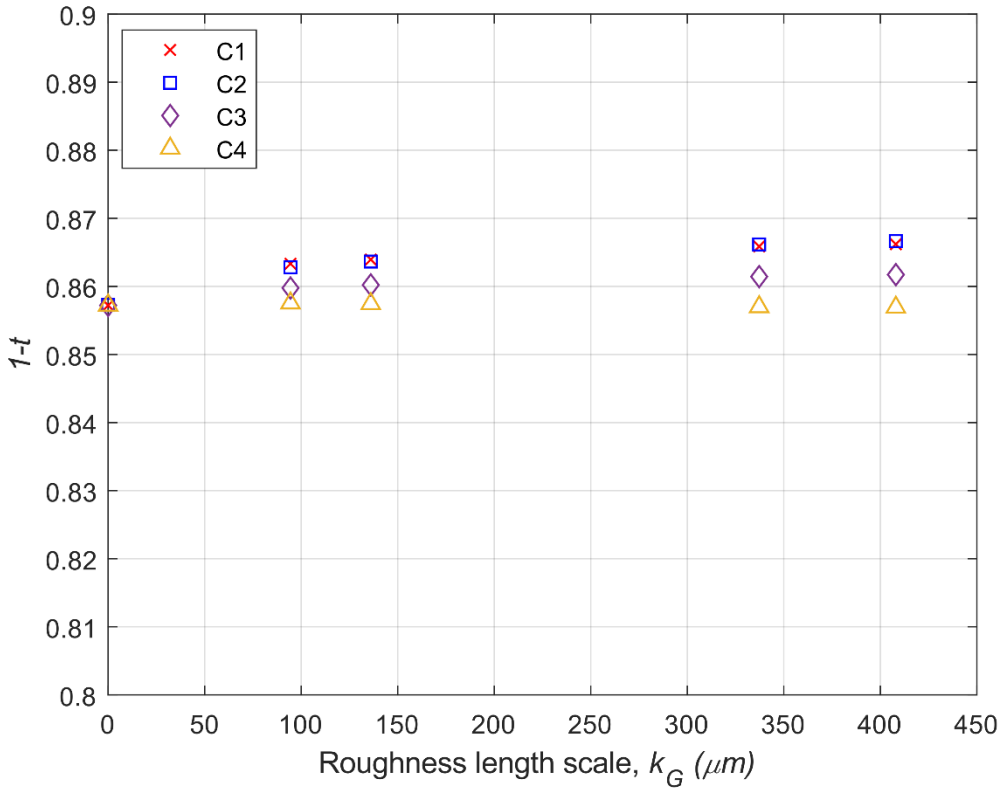

Figure 16 Thrust deduction coefficient, $\mathbf{1-t}$ at self-propulsion point against roughness length scales of surface conditions

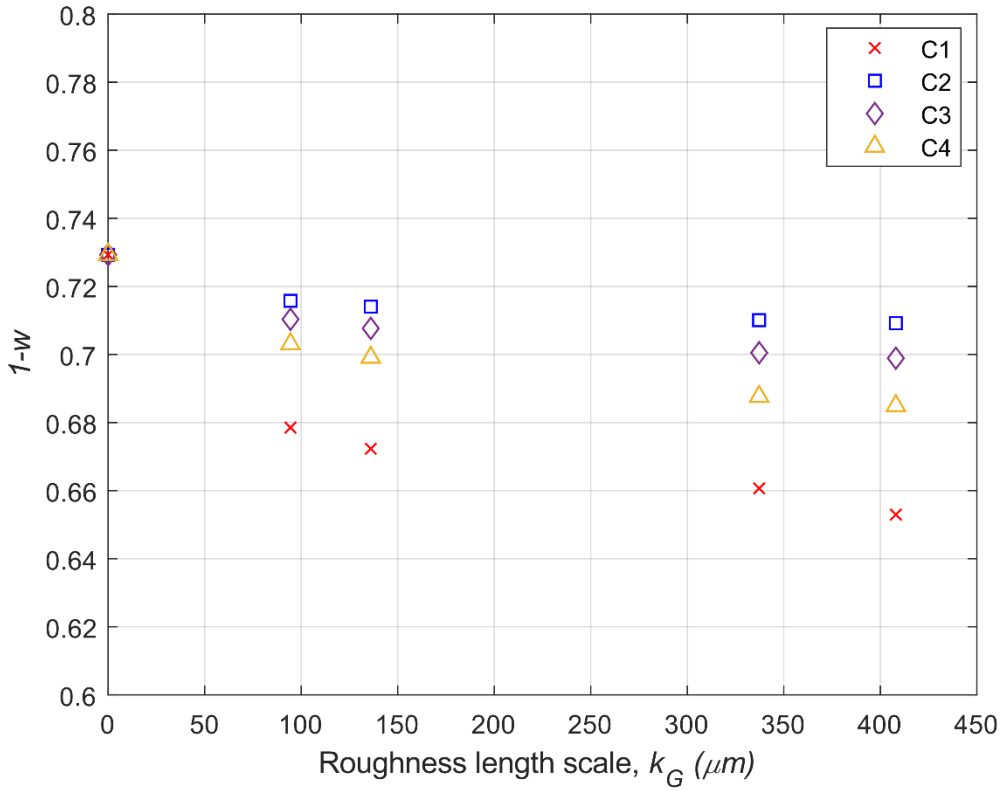

Figure 17 Wake fraction coefficient, $\mathbf{1-w}$ in self-propulsion point against roughness length scales of surface conditions

Figure 16 and Figure 17 show the changes in the $1-t$ and $1-w$ under the varying roughness conditions, respectively. The similarity between the increases in P_D and R_T can be attributed to the fact that the effect of roughness on $1-t$ is negligible, with only a 1.09% difference overall. On the other hand, the presence of roughness has a considerable effect on the $1-w$. Thus, it causes a decrease in $1-w$, ranging from -1.86% for C2 up to -10.47% for C1. The effective wake shows a substantial decrease due to the thicker boundary layer as the ship hull is rough. Therefore, $1-w$ decreases depending on the decrease in the V_a. As seen in equation 15, the decrease in the $1-w$ positively affects η_H as the presence of roughness does not affect the $1-t$. Thus, the increase in η_H ranges from 2.55% for C2 up to 12.86% for C1, as shown in Figure 18.

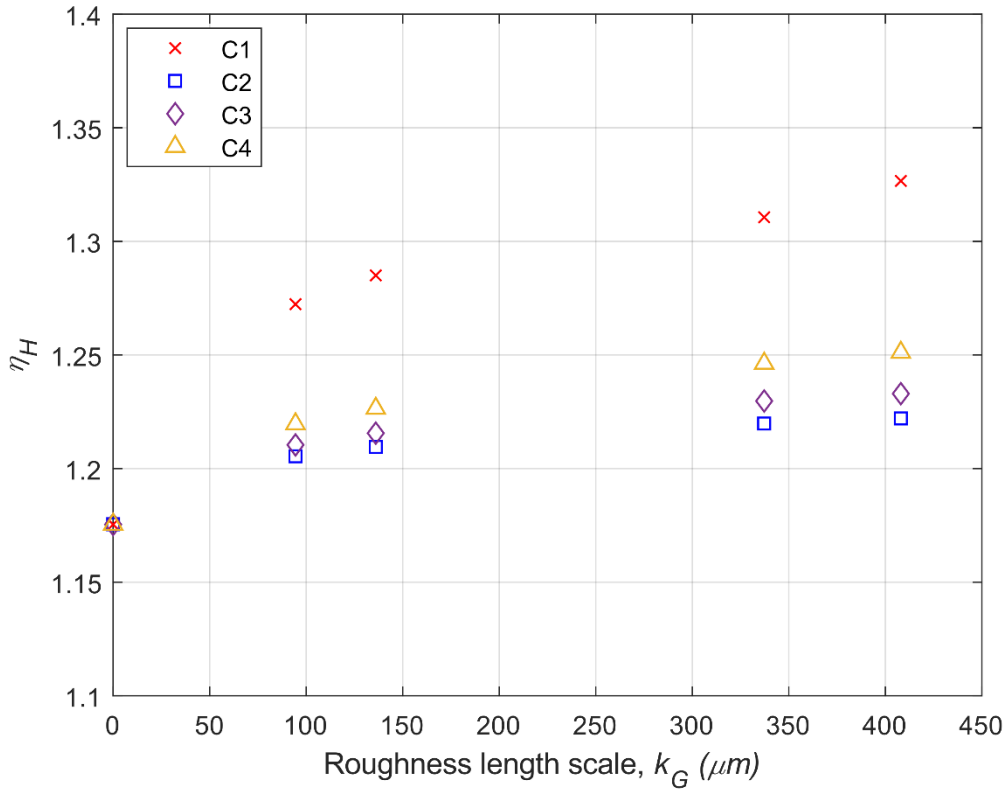

Figure 18 Hull efficiency, $\boldsymbol{\eta_H}$ at self-propulsion point against roughness length scales of surface conditions

The results indicate that surface roughness drastically changes the flow around the ship and has detrimental effects on the flow velocity on the propeller operating point. Figure 19 shows the effect of roughness on η_R. As seen from the figure η_R values decrease with the increasing roughness length scales. However, this decrease is negligible, with only -1.37% for the most severe condition.

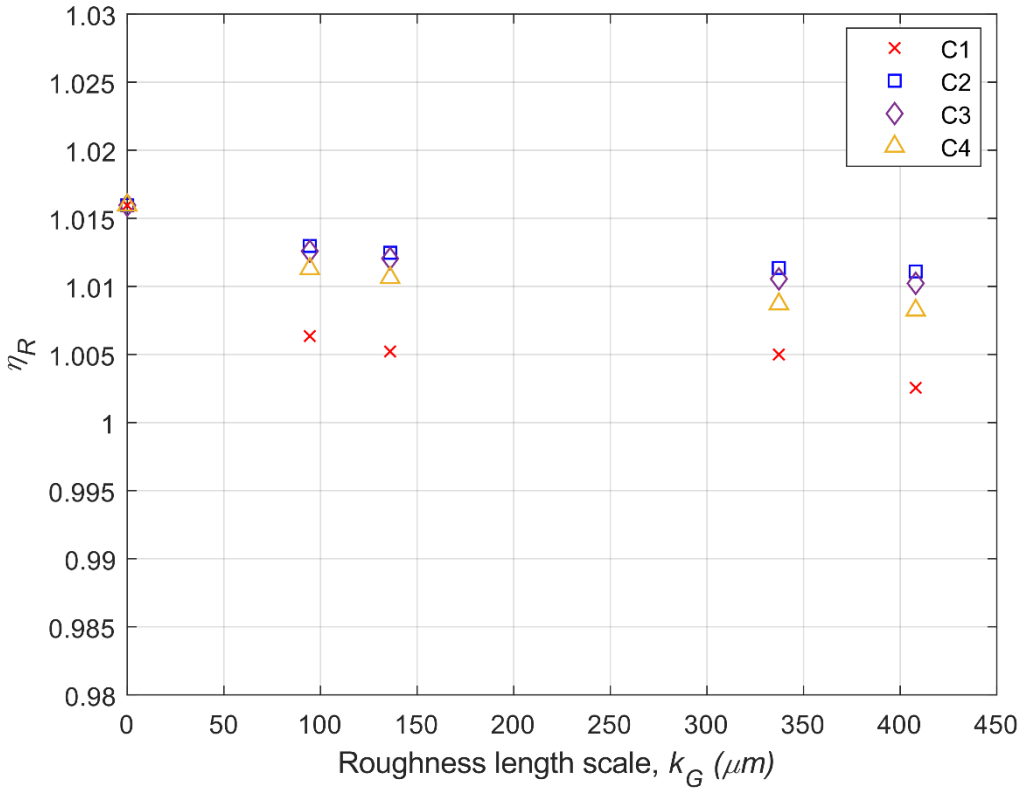

Figure 19 Relative rotative efficiency, $\boldsymbol{\eta_R}$ at self-propulsion point against roughness length scales of surface conditions

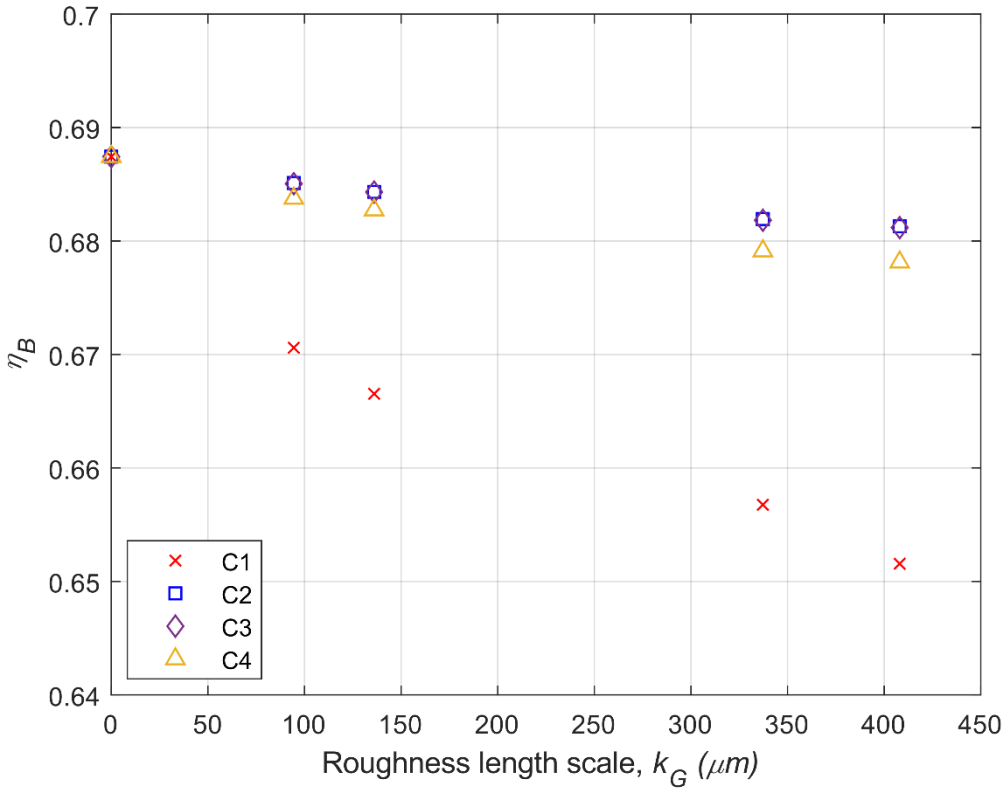

Figure 20 Propeller efficiency behind the hull, $\boldsymbol{\eta_B}$ at self-propulsion point against roughness length scales of surface conditions

Figure 20 shows the change in the propeller behind hull efficiency, η_B with increasing roughness length scales. As seen from the figure η_B decreases with the effect of roughness. As both $\eta_R$and η_O decrease, η_B also reduces due to the effect of roughness, as given in equation 12.

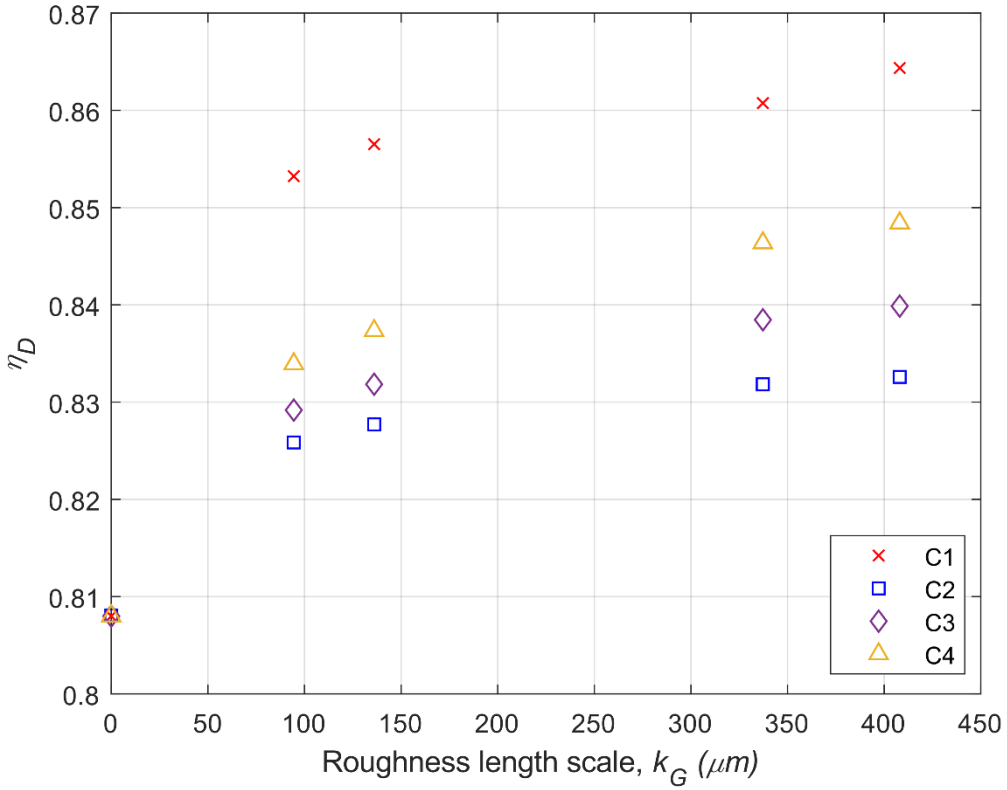

Figure 21 Propulsive efficiency, $\boldsymbol{\eta_D}$ at self-propulsion point against roughness length scales of surface conditions

Finally, Figure 21 illustrates the effect of hull roughness on the propulsive efficiency, η_D, under varying roughness conditions which indicates an increase over the smooth hull for all roughness conditions. The increase in the η_D is predicted to be in a range from 2.2% for C2 up to 6.97% for C1, as given in Tables A5-A8. Since the increases in the η_H (i.e. 12.86%) comparatively higher than the decreases in the η_R (i.e.-1.32%) and η_O (i.e. -3.95%), η_D increases with the effect of roughness for all cases, as given in equation 16.

6 CONCLUSIONS

The effect of barnacle type biofouling on powering and self-propulsion characteristics of a submarine is investigated using a CFD model. The CFD analyses are conducted for varying hull roughness conditions, including heterogeneous distributed conditions (C2: forward section rough, C3: midsection rough and C4: aft section rough) and the homogenous distributed conditions (C0: smooth and C1: fully rough conditions) as shown in Figure 4. In general, the results of this investigation suggest that:

- The increases in delivered power, P_D are calculated to be in a range from 11.49% for C2 up to 64.73% for C1. As expected, C1 is the most severely affected condition as the whole submarine hull is in rough condition. There is no discernible difference between the P_D values of C3 and C4, which means roughness distribution on the mid-section or

aft section has a similar effect on the P_D. On the other hand, C1 causes comparatively higher increases in the P_D as shown in Table A1-A4. A similar trend is observed in the R_T with the increases ranged from 14.07% for C3 up to 74.39% for C1.

- As the roughness increases the shaft speed, n decreases while the advance velocity, V_a decreases due to the presence of a thicker boundary layer, which result in a significant reduction in the J ranging from -3.72% for C3 up to -16.73% for C1. Although no considerable difference is found between the C2, C3 and C4, roughness presence at the aft section of the submarine causes a slightly higher decrease in J. It is important to note that such a substantial change in the J values is undesirable, as the marine propellers are designed to operate in a defined J to have optimum efficiency.

- The roughness decreased the $1-w$ values in a range from -1.86% for C2 up to -10.47% for C1. The results stated that the roughness distribution close to the aft section of the submarine causes a higher decrease in the $1-w$, as the presence of roughness at the aft changes the water velocity more dominantly than the mid and forward section. The severest decreases in the $1-w$ values are calculated to be -2.76% for C2, -4.17% for C3 and -6.08% for C4.

- The results of the study indicate that the effect of barnacle type roughness and heterogeneous distribution on the $1-t$ and η_R is negligible. The biggest change in the $1-t$ was calculated to be only ~1%, whereas this number altered to -1.3% for η_R.

- Although the roughness decreases both η_R and η_O, the increase in the η_H is dominant and thus causes an increase in a range from 2.2% up to 6.97% in the η_D. It is of note that the effect of roughness increases the propulsive efficiency if the only hull is fouled and the propeller is in smooth condition.

The investigation provided practical and helpful judgement to understand the effect of barnacle type roughness on the full-scale submarine's self-propulsion characteristics. These findings can be useful for evaluating the required power and fuel consumption of a submarine fouled with barnacles. However, it is essential to note that these fouling conditions are specific, and it is challenging to catch the same fouling conditions for the submarines operating at world seas.

For this reason, as a further study, a time-dependent biofouling growth model (Uzun et al., 2019) can be used to predict the fouling condition of real operating submarines. CFD studies combined with a time-dependent biofouling growth model can be beneficial to optimise the maintenance schedule of submarines.

The above-stated findings indicated that surface roughness substantially changes the propeller inflow and hence propeller loading. Inevitably, the change in propeller loading will cause alterations in the underwater radiated noise (URN) induced by the propeller, which is especially critical for the submarines. For this reason, the studies should be further extended to include the effect of the biofouling roughness on the propeller radiated URN both in the model and full-scale submarines.

Appendix

Table A 1 The effect of roughness on the $R_T, T, Q, n, J, P_E, P_T$ and P_D for the configuration C1

Roughness Length scale	R_T, kN (*Without propeller*)	T, kN	Q, kNm	n, rps	J	P_E, kW	P_T, kW	P_D, kW
0 (S)	394.700	460.446	598.642	1.336	0.893	4060.6	3454.7	5025.6
94	574.163(45.46%)	665.055(44.43%)	790.966(32.12%)	1.393(4.26%)	0.7969(-10.76%)	5906.9(45.47%)	4642.5(34.38%)	6923(37.75%)
136	600.837(52.22%)	695.465(51.04%)	819.075(36.82%)	1.402(4.95%)	0.7844(-12.16%)	6181.4(52.23%)	4810.3(39.24%)	7216.9(43.6%)
337	677.473(71.64%)	782.427(69.92%)	898.573(50.11%)	1.434(7.34%)	0.7536(-15.60%)	6969.8(71.64%)	5318(53.93%)	8097.4(61.12%)
408	695.536(76.21%)	802.973(74.39%)	917.149(53.2%)	1.436(7.52%)	0.7436(-16.73%)	7155.6(76.22%)	5394(56.13%)	8278.6(64.73%)

Table A 2 The effect of roughness on the $R_T, T, Q, n, J, P_E, P_T$ and P_D for the configuration C2

Roughness Length scale	R_T, kN (*Without propeller*)	T, kN	Q, kNm	n, rps	J	P_E, kW	P_T, kW	P_D, kW
0 (S)	394.700	460.446	598.642	1.336	0.893	4060.6	3454.7	5025.6
94	467.190(18.37%)	541.469(17.59%)	677.844(13.23%)	1.366(2.27%)	0.857(-4.04%)	4806.4(18.35%)	3987.3(15.41%)	5819.9(15.8%)
136	478.401(21.21%)	553.939(20.3%)	690.067(15.27%)	1.371(2.64%)	0.852(-4.61%)	4921.7(21.19%)	4069.2(17.78%)	5946.3(18.32)
337	511.103(29.49%)	590.084(28.15%)	725.519(21.19%)	1.386(3.78%)	0.838(-6.18%)	5258.2(29.48%)	4310.7(24.77%)	6321.2(25.78%)
408	518.905(31.47%)	598.739(30%)	733.993(22.6%)	1.390(4.06%)	0.834(-6.55%)	5338.5(31.45%)	4368.4(26.45%)	6411.9(27.58%)

Table A 3 The effect of roughness on the $R_T, T, Q, n, J, P_E, P_T$ and P_D for the configuration C3

Roughness Length scale	R_T, kN (*Without propeller*)	T, kN	Q, kNm	n, rps	J	P_E, kW	P_T, kW	P_D, kW
0 (S)	394.700	460.446	598.642	1.336	0.893	4060.6	3454.7	5025.6
94	451.597(14.42%)	525.256(14.07%)	659.754(10.2%)	1.351(1.16%)	0.859(-3.72%)	4646(14.41%)	3838.4(11.11%)	5603.2(11.49%)
136	460.531(16.68%)	535.367(16.27%)	669.311(11.8%)	1.354(1.37%)	0.854(-4.27%)	4737.9(16.68%)	3897.6(12.82%)	5695.7(13.33%)
337	486.382(23.23%)	564.622(22.62%)	697.001(16.43%)	1.362(1.99%)	0.841(-5.82%)	5003.9(23.23%)	4069.1(17.78%)	5967.9(18.75%)
408	492.538(24.79%)	571.569(24.13%)	703.571(17.52%)	1.364(2.15%)	0.837(-6.18%)	5067.2(24.79%)	4109.8(18.96%)	6033.3(20.05%)

Table A 4 The effect of roughness on the $R_T, T, Q, n, J, P_E, P_T$ and P_D for the configuration C4

Roughness Length scale	R_T, kN (*Without propeller*)	T, kN	Q, kNm	n, rps	J	P_E, kW	P_T, kW	P_D, kW
0 (S)	394.700	460.446	598.642	1.336	0.893	4060.6	3454.7	5025.6
94	454.730(15.21%)	530.289(15.16%)	663.005(10.75%)	1.346(0.79%)	0.854(-4.35%)	4678.2(15.21%)	3835.7(11.03%)	5609.8(11.62%)
136	464.174(17.60%)	541.344(17.57%)	673.100(12.43%)	1.348(0.93%)	0.848(-5.02%)	4775.4(17.6%)	3893.6(12.70%)	5703.1(13.48%)
337	491.779(24.60%)	573.844(24.63)	702.624(17.37%)	1.354(1.34%)	0.831(-6.96%)	5059.4(24.60%)	4059.6(17.51%)	5977.8(18.95%)
408	498.452(26.29%)	581.686(26.33%)	709.713(18.55%)	1.355(1.45%)	0.827(-7.42%)	5128.1(26.29%)	4098.8(18.64%)	6044.3(20.27%)

Table A 5 The effect of biofouling roughness on the self-propulsion characteristics for the configuration C1

Roughness Length scale	$1-w$	$1-t$	η_H	η_R	η_O	η_B	η_D
0 (S)	0.7293	0.8572	1.1754	1.0159	0.6766	0.6874	0.8079
94	0.6785 (-6.96%)	0.8633 (0.71%)	1.272 (8.25%)	1.006(-0.94%)	0.6663(-1.52%)	0.6706(-2.45%)	0.8532(5.60%)
136	0.6723(-7.81%)	0.8639 (0.78%)	1.285 (9.33%)	1.005(-1.05%)	0.6631(-2%)	0.6665(-3.04%)	0.8565(6.01%)
337	0.6606(-9.41%)	0.8658 (1.01%)	1.311 (11.50%)	1.004(-1.07%)	0.6535(-3.42%)	0.6567(-4.46%)	0.8607(6.53%)
408	0.6529(-10.47%)	0.8662 (1.04%)	1.327 (12.86%)	1.003(-1.32%)	0.6499(-3.95%)	0.6515(-5.22%)	0.8643(6.97%)

Table A 6 The effect of biofouling roughness on the self-propulsion characteristics for the configuration C2

Roughness Length scale	$1-w$	$1-t$	η_H	η_R	η_O	η_B	η_D
0 (S)	0.7293	0.8572	1.1754	1.0159	0.6766	0.6874	0.8079
94	0.7157(-1.86%)	0.8628(0.64%)	1.2054(2.55%)	1.0129(-0.29%)	0.6763(-0.04%)	0.6851(-0.34%)	0.8258(2.20%)
136	0.7140(-2.09%)	0.8636(0.74%)	1.2095(2.89%)	1.0125(-0.34%)	0.6759(-0.11%)	0.6843(-0.45%)	0.8277(2.43%)
337	0.7101(-2.63%)	0.8662(1.04%)	1.2198(3.77%)	1.0114(-0.45%)	0.6743(-0.35%)	0.6819(-0.80%)	0.8318(2.94%)

408	0.7092(-2.76%)	0.8666(1.09%)	1.2221(3.96%)	1.0111(-0.47%)	0.6738(-0.42%)	0.6813(-0.90%)	0.8326(3.03%)

Table A 7 The effect of biofouling roughness on the self-propulsion characteristics for the configuration C3

Roughness Length scale	$1-w$	$1-t$	η_H	η_R	η_O	η_B	η_D
0 (S)	0.7293	0.8572	1.1754	1.0159	0.6766	0.6874	0.8079
94	0.7103(-2.60%)	0.8597(0.29%)	1.2104(2.98%)	1.0126(-0.33%)	0.6765(-0.01%)	0.6851(-0.34%)	0.8292(2.62%)
136	0.7076(-2.97%)	0.8602(0.35%)	1.2156(3.42%)	1.0120(-0.38%)	0.6762(-0.07%)	0.6843(-0.45%)	0.8318(2.95%)
337	0.7005(-3.95%)	0.8614(0.49%)	1.2297(4.62%)	1.0105(-0.53%)	0.6747(-0.28%)	0.6818(-0.82%)	0.8384(3.77%)
408	0.6989(-4.17%)	0.8617(0.52%)	1.2329(4.90%)	1.0102(-0.56%)	0.6743(-0.35%)	0.6812(-0.91%)	0.8398(3.94%)

Table A 8 The effect of biofouling roughness on the self-propulsion characteristics for the configuration C4

Roughness Length scale	$1-w$	$1-t$	η_H	η_R	η_O	η_B	η_D
0 (S)	0.7293	0.8572	1.1754	1.0159	0.6766	0.6874	0.8079
94	0.7031(-3.59%)	0.8575(0.037%)	1.2196(3.76%)	1.0113(-0.46%)	0.6761(-0.08%)	0.6838(-0.54%)	0.8339(3.21%)
136	0.6991(-4.14%)	0.8574(0.026%)	1.2265(4.34%)	1.0106(-0.52%)	0.6755(-0.16%)	0.6827(-0.68%)	0.8373(3.63%)
337	0.6876(-5.71%)	0.8569(-0.026%)	1.2463(6.03%)	1.0087(-0.71%)	0.6733(-0.49%)	0.6791(-1.21%)	0.8464(4.75%)
408	0.6849(-6.08%)	0.8569(-0.034%)	1.2511(6.44%)	1.0082(-0.76%)	0.6726(-0.59%)	0.6781(-1.35%)	0.8484(5%)

7 ACKNOWLEDGEMENT

The second author is sponsored by the Stone Marine Propulsion Ltd of the UK and the University of Strathclyde during his PhD study. Results were obtained using the ARCHIE-WeSt High-Performance Computer (www.archie-west.ac.uk) based at the University of Strathclyde. This work is partially supported by MarEd (Maritime Education for Energy Efficiency) Project by European Commission under the framework of Erasmus+ KA2 Cooperation for Innovation and the Exchange of Good Practices, KA202 Strategic Partnership for vocational education and training (Grant Number: 2018-1-TR01-KA202-058717)

CRediT authorship contribution statement

Dogancan Uzun: Conceptualisation, Software, Methodology, Data curation, Formal analysis, Visualisation, Writing - original draft, Writing - review & editing. **Savas Sezen:** Conceptualisation, Software, Methodology, Data curation, Formal analysis, Visualisation, Writing - original draft, Writing - review & editing. **Mehmet Atlar:** Conceptualisation, Funding acquisition, Methodology, Writing - review & editing, Supervision. **Osman Turan:** Conceptualisation, Funding acquisition, Methodology, Writing - review & editing, Supervision

8 REFERENCES

Andersson, J., Oliveira, D.R., Yeginbayeva, I., Leer-Andersen, M., Bensow, R.E., 2020. Review and comparison of methods to model ship hull roughness. Applied Ocean Research 99.

Carrica, P.M., Castro, A.M., Stern, F., 2010. Self-propulsion computations using a speed controller and a discretized propeller with dynamic overset grids. Journal of marine science and technology 15 (4), 316-330.

Castro, A.M., Carrica, P.M., Stern, F., 2011. Full scale self-propulsion computations using discretized propeller for the KRISO container ship KCS. Computers & Fluids 51 (1), 35-47.

Celik, I., Ghia, K.N., Roache, P.J., Freitas, C.J., Coleman, H., E., R.P., 2008. Procedure for Estimation and Reporting of Uncertainty Due to Discretization in CFD Applications. Journal of Fluids Engineering 130 (7).

Chase, N., Carrica, P.M., 2013. Submarine propeller computations and application to selfpropulsion of DARPA Suboff. Ocean Engineering 60, 68-80.

Clauser, F.H., 1954. Turbulent Boundary Layers in Adverse Pressure Gradients. Journal of the Aeronautical Sciences 21 (2), 91-108.

Davidson, I.C., Brown, C.W., Sytsma, M.D., Ruiz, G.M., 2009. The role of containerships as transfer mechanisms of marine biofouling species. Biofouling 25 (7), 645-655.

Demirel, Y.K., Khorasanchi, M., Turan, O., Incecik, A., Schultz, M.P., 2014. A CFD model for the frictional resistance prediction of antifouling coatings. Ocean Engineering 89, 21-31.

Demirel, Y.K., Song, S., Turan, O., Incecik, A., 2019. Practical added resistance diagrams to predict fouling impact on ship performance. Ocean Engineering 186.

Demirel, Y.K., Turan, O., Incecik, A., 2017. Predicting the effect of biofouling on ship resistance using CFD. Applied Ocean Research 62, 100-118.

Denny, M., 1951. B.S.R.A. resistance experiments on the Lucy Ashton: part I – full-scale measurements. Trans INA 93, 40-57.

Farkas, A., Degiuli, N., Martić, I., 2018. Towards the prediction of the effect of biofilm on the ship resistance using CFD. Ocean Engineering 167, 169-186.

Farkas, A., Degiuli, N., Martić, I., 2021. Assessment of the effect of biofilm on the ship hydrodynamic performance by performance prediction method. International Journal of Naval Architecture and Ocean Engineering 13, 102-114.

Farkas, A., Song, S., Degiuli, N., Martić, I., Demirel, Y.K., 2020. Impact of biofilm on the ship propulsion characteristics and the speed reduction. Ocean Engineering 199.

Flack, K.A., Schultz, M.P., Shapiro, T.A., 2005. Experimental support for Townsend's Reynolds number similarity hypothesis on rough walls. Physics of Fluids 17 (3), 035102.

García, S., Trueba, A., Boullosa-Falces, D., Islam, H., Guedes Soares, C., 2020. Predicting ship frictional resistance due to biofouling using Reynolds-averaged Navier-Stokes simulations. Applied Ocean Research 101, 102203.

Granville, P.S., 1958. The frictional resistance and turbulent boundary layer of rough surfaces.Journal of ship research 2 (04), 52-74.

Grigson, C., 1992. Drag losses of new ships caused by hull finish. Journal of Ship Research 36 (02), 182-196.

Groves, N.C., Huang, T.T., Chang, M.S., David Taylor Research, C., 1989. Geometric characteristics of DARPA suboff models : (DTRC model nos. 5470 and 5471). David Taylor Research Center, Bethesda, MD.

Hama, F.R., 1954. Boundary Layer characteristics for smooth and rough surfaces.

ITTC, 2002. Testing and extrapolation methods, performance propulsion test (Recommended Procedures and Guidelines; report 7.5-02-03-01.1), Rio de Janeiro.

ITTC, 2011. Recommended Procedures and Guideline Practical Guidelines for Ship CFD Applications, 2011-7.5-0.3, ITTC.

Kempf, G., 1936. A Study of Ship Performance in Smooth and Rough Water. Trans. Soc. Nav. Arch. and Mar. Eng. 44, 195-227.

Khor, Y.S., Xiao, Q., 2011. CFD simulations of the effects of fouling and antifouling. Ocean Engineering 38 (10), 1065-1079.

Krogstadt, P.Å., Antonia, R.A., 1999. Surface roughness effects in turbulent boundary layers. Experiments in fluids 27 (5), 450-460.

Kinaci, O.K., Gokce, M.K., Alkan, A.D., Kukner, A., 2018. On self-propulsion assessment of marine vehicles. Brodogr. Teor. Praksa Brodogr. Pomor. Teh. 69, 29–51. https://doi.org/10.21278/brod69403.

Liu, H.-L., Huang, T.T., 1998. Summary of DARPA SUBOFF experimental program data. NAVAL SURFACE WARFARE CENTER CARDEROCK DIV BETHESDA MD HYDROMECHANICS ….

Menter, F.R., 1994. Two-equation eddy-viscosity turbulence models for engineering applications. AIAA Journal 32 (8), 1598-1605.

Mikkelsen, H., Walther, J.H., 2020. Effect of roughness in full-scale validation of a CFD model of self-propelled ships. Applied Ocean Research 99, 102162.

Murphy, E.A.K., Barros, J.M., Schultz, M.P., Flack, K.A., Steppe, C.N., Reidenbach, M.A., 2018. Roughness effects of diatomaceous slime fouling on turbulent boundary layer hydrodynamics. Biofouling 34 (9), 976-988.

ONR, 2009. Office of Naval Research Hull Bug video transcript.

Ozden, Y.A., Ozden, M.C., Demir, E., Kurdoglu, S., 2019. Experimental and numerical investigation of DARPA suboff submarine propelled with INSEAN E1619 propeller for self-propulsion. J. Ship Res. 63, 235–250

Östman, A.; Koushan, K.; Savio, L. Study on additional ship resistance due to roughness using CFD. In Proceedings of the 4th Hull Performance & Insight Conference (HullPIC'19), Gubbio, Italy, 6–8 May 2019.

Putnam, D., 2016. OHIO Class External Hull Antifouling, pp. Navy SBIR 2016.2011 - Topic N2161-2044.

Roache, P.J., 1997. QUANTIFICATION OF UNCERTAINTY IN COMPUTATIONAL FLUID DYNAMICS. Annual Review of Fluid Mechanics 29 (1), 123-160.

Roache, P.J., 1998. Verification of Codes and Calculations. AIAA Journal 36 (5), 696-702.
Schultz, M., Flack, K., 2005. Outer layer similarity in fully rough turbulent boundary layers. Experiments in fluids 38 (3), 328-340.

Schultz, M.P., 2004. Frictional Resistance of Antifouling Coating Systems. Journal of Fluids Engineering 126 (6), 1039-1047.

Schultz, M.P., 2007. Effects of coating roughness and biofouling on ship resistance and powering. Biofouling 23 (5), 331-341.

Schultz, M.P., Bendick, J.A., Holm, E.R., Hertel, W.M., 2011. Economic impact of biofouling on a naval surface ship. Biofouling 27 (1), 87-98.

Schultz, M.P., Flack, K.A., 2003. Turbulent Boundary Layers Over Surfaces Smoothed by Sanding. Journal of Fluids Engineering 125 (5), 863-870.

Sezen, S., Dogrul, A., Delen, C., Bal, S., 2018. Investigation of self-propulsion of DARPA Suboff by RANS method. Ocean Engineering 150, 258-271.

Sezen, S., Delen, C., Dogrul, A., Atlar, M. An investigation of scale effects on the selfpropulsion characteristics of a submarine, Appl. Ocean Res. 113 (2021) 102728. https://doi.org/10.1016/j.apor.2021.102728.

Siemens, 2020. Star-CCM+ User Guide Version 15.02.

Song, S., Demirel, Y.K., Atlar, M., 2019. An investigation into the effect of biofouling on the ship hydrodynamic characteristics using CFD. Ocean Engineering 175, 122-137.

Song, S., Demirel, Y.K., Atlar, M., 2020. Penalty of hull and propeller fouling on ship selfpropulsionperformance. Applied Ocean Research 94, 102006.

Song, S., Ravenna, R., Dai, S., DeMarco Muscat-Fenech, C., Tani, G., Demirel, Y.K., Atlar, M., Day, S., Incecik, A., 2021. Experimental investigation on the effect of heterogeneous hull roughness on ship resistance. Ocean Engineering 223, 108590.

Song, S., Demirel, Y.K., De Marco Muscat-Fenech, C., Sant, T., Villa, D., Tezdogan, T., Incecik, A., 2021a. Investigating the Effect of Heterogeneous Hull Roughness on Ship Resistance Using CFD. Journal of Marine Science and Engineering 9 (2).

Speranza, N., Kidd, B., Schultz, M.P., Viola, I.M., 2019. Modelling of hull roughness. Ocean Engineering 174, 31-42.

Stern, F., Wilson, R., Shao, J., 2006. Quantitative V&V of CFD simulations and certification of CFD codes. International journal for numerical methods in fluids 50 (11), 1335-1355.

Townsend, A., 1980. The structure of turbulent shear flow. Cambridge university press.

Townsin, R., Dey, S., 1990. The correlation of roughness drag with surface characteristics, Proceedings of the RINA international workshop on marine roughness and drag.

Townsin, R.L., 2003. The ship hull fouling penalty. Biofouling 19 Suppl, 9-15.

Uzun, D., Demirel, Y.K., Coraddu, A., Turan, O., 2019. Time-dependent biofouling growth model for predicting the effects of biofouling on ship resistance and powering. Ocean Engineering 191.

Uzun, D., Ozyurt, R., Demirel, Y.K., Turan, O., 2020. Does the barnacle settlement pattern affect ship resistance and powering? Applied Ocean Research 95.

Uzun, D., Sezen, S., Ozyurt, R., Atlar, M., Turan, O., 2021. A CFD study: Influence of biofouling on a full-scale submarine. Applied Ocean Research 109, 102561.

Vargas, A.; Shan, H.; Holm, E. Using CFD to predict ship resistance due to biofouling, and plan hull maintenance. In Proceedings of the 4th Hull Performance & Insight Conference (HullPIC'19), Gubbio, Italy, 6–8 May 2019.

Vaz, G., Toxopeus, S., Holmes, S., 2010. Calculation of manoeuvring forces on submarines using two viscous-flow solvers, International Conference on Offshore Mechanics and Arctic Engineering, pp. 621-633.

Yeginbayeva, I.A., Atlar, M., Turkmen, S., Chen, H., 2020. Effects of 'in-service' conditions – mimicked hull roughness ranges and biofilms – on the surface and the hydrodynamic characteristics of foul-release type coatings. Biofouling 36 (9), 1074-1089.

Yeginbayeva, I.A., Granhag, L., Chernoray, V., 2018. Review and historical overview of experimental facilities used in hull coating hydrodynamic tests. Proceedings of the Institution of Mechanical Engineers, Part M: Journal of Engineering for the Maritime Environment 233 (4), 1240-1259.